The important roles of surface tension and growth rate in the contribution of new particle formation (NPF) to cloud condensation nuclei (CCN) number concentration: evidence from field measurements in southern China

Mingfu Cai[1,2,3,4], Baoling Liang[3], Qibin Sun[3], Li Liu[4], Bin Yuan[1,2*], Min Shao[1,2], Shan Huang[1,2], Yuwen Peng[1,2], Zelong Wang[1,2], Haobo Tan[4], Fei Li[4,6], Hanbin Xu[3], Duohong Chen[7], and Jun Zhao[3,5,8*]

[1] Institute for Environmental and Climate Research, Jinan University, Guangzhou, Guangdong 511443, China

[2] Guangdong-Hongkong-Macau Joint Laboratory of Collaborative Innovation for Environmental Quality, Guangzhou, Guangdong 511443, China

[3] School of Atmospheric Sciences, Guangdong Province Key Laboratory for Climate Change and Natural Disaster Studies, and Institute of Earth Climate and Environment System, Sun Yat-sen University, Zhuhai, Guangdong 519082, China

[4] Institute of Tropical and Marine Meteorology/Guangdong Provincial Key Laboratory of Regional Numerical Weather Prediction, CMA, Guangzhou 510640, China

[5] Southern Marine Science and Engineering Guangdong Laboratory (Zhuhai), Zhuhai, Guangdong 519082, China

[6] Laboratory of straits meteorology, Xiamen, Guangdong 361012, China

[7] Guangdong Environmental Monitoring Center, Guangzhou 510308, China

[8] Guangdong Provincial Observation and Research Station for Climate Environment and Air Quality Change in the Pearl River Estuary, Guangzhou, Guangdong 510275, China

*Corresponding authors: Bin Yuan (byuan@jnu.edu.cn) and Jun Zhao (zhaojun23@mail.sysu.edu.cn)

Abstract.

The contribution of new particle formation (NPF) to cloud condensation nuclei (CCN) number concentration varies largely under different environments and depends on several key factors such as formation rate (J), growth rate (GR), distribution of preexisting particles and properties of new particles during NPF events. This study investigates the contribution of NPF to the N_{CCN} and its controlling factors based on measurements conducted at the Heshan supersite, in the Pearl River Delta (PRD) region of China during fall-time 2019. The size-resolved cloud condensation nuclei activity and size-resolved particle hygroscopicity were measured by a cloud condensation nuclei counter (CCNc) and a hygroscopic tandem differential mobility analyzer (HTDMA), respectively, along with a scanning mobility particle sizer (SMPS) and a diethylene glycol scanning mobility particle sizer (DEG-SMPS) for particle number size distribution (PNSD). A typical NPF event on 29th October was chosen to investigate the contribution of the NPF to N_{CCN} under several supersaturation ratios. Two particle properties (hygroscopicity and surface tension) affect CCN activation with the latter being more important in terms of the CCN concentration (N_{CCN}). A lower value of surface tension (i.e., 0.06 N m^{-1}) than pure water assumption (0.073 N m^{-1}) could increase the N_{CCN} at SS=1.0% by about 20% during non-event period and by about 40% during the event. In addition, an earlier peak time corresponding to a lower critical diameter (D_{50}) was also observed. The results show that high formation rate, growth rate, and low background particle concentration lead to high number concentrations of newly-formed particles. The high growth rate was found to have the most significant impact on the N_{CCN} which can be attributed to the fact that a higher growth rate can grow particles to the CCN size in a shorter time before they are scavenged by pre-existing particles. Two other NPF events (an event on 18th October in this campaign and an event on 12th December, 2014 in Panyu) were chosen to perform sensitivity tests

2

48 under different scenarios (growth rate, formation rate, and background particle concertation). The

49 calculated N_{CCN} at SS=1.0% on 12th December, 2014 was significantly lower than that from the other

50 two events. The event on 12th December was re-simulated using high growth rate taken from the event

51 on 18th October which resulted in similar CCN concentrations between the two events (12th December

52 and 18th October), implying that the growth rate is the major impact factor for CCN activation. Our

53 results highlight the importance of growth rate and surface tension when evaluating the contribution of

54 NPF to the N_{CCN}.

55 **1   Introduction**

56   Atmospheric particles have direct effects on global climate by adsorbing and scattering solar

57 radiation, while they can act as cloud condensation nuclei (CCN) and exert influences on cloud

58 formation, life cycle, and albedo, hence indirectly affect the global radiation balance. In general,

59 atmospheric particles have a cooling effect on the global climate with the highest uncertainty among all

60 the climatic forcings (Stocker et al., 2013). The relationship between the CCN number concentration

61 (N_{CCN}) and its climatic effect represents one of the major uncertainties. It is hence essential to carry out

62 field measurements to investigate the CCN activity and its major impact factor.

63   New particle formation (NPF) as an important source of global atmospheric particles, is frequently

64 observed in various atmospheric environments, including forest, urban, marine, and agricultural regions

65 (Kulmala et al., 2004). Once formed, the particles can grow to the CCN sizes (50-100 nm) within a few

66 hours and contribute significantly to the N_{CCN} (Leng et al., 2014; Spracklen et al., 2008; Dameto de

67 España et al., 2017). The extent to which newly-formed particles can contribute to the N_{CCN} is

68 controlled by many factors, including formation rate (J), growth rate (GR), background particle number

3

size distribution (PNSD), and properties of the particles. The formation rate is defined as a flux of newly-formed particles at a threshold diameter and is usually used to describe how many particles are produced into the atmosphere during an event. The growth rate (GR) represents the diameter change of the particles in a certain time period, and particles with a higher GR will grow to the CCN sizes in a shorter time. The background PNSD controls the scavenging of the newly-formed particles, and the high concentration of pre-existing particles will efficiently scavenge these particles before they can grow to the CCN sizes. The properties of the particles (e.g., chemical composition, hygroscopicity, and surface tension) affect their ability of acting as CCN. In general, particles containing a higher fraction of inorganic matter or water-soluble organics are more hygroscopic and more easily activated due to a lower critical diameter (D_{50}). Recent studies showed that surfactant effects of organic matter were found on the particle surface which could lead to an increase of the CCN activity (Ovadnevaite et al., 2017; Cai et al., 2018; Liu et al., 2018). The contribution of NPF to N_{CCN} is difficult to be quantitatively evaluated and currently the major impact factors are not fully understood, which becomes a challenging in quantification of the climatic forcing of NPF events.

NPF event is well known to have an important contribution to the N_{CCN}, while a wide range of N_{CCN} during NPF events was reported in the literature. Yue et al. (2011) showed that the N_{CCN} during NPF events was increased by a factor of 0.4-6 in Beijing. However, much less (a factor of 1.17-1.88) increase of the N_{CCN} was observed during NPF events in Shanghai (Leng et al., 2014). The results from Ma et al. (2016) showed that the N_{CCN} was significantly impacted by the hygroscopicity of newly-formed particles during NPF events in the North China Plain (NCP). Yu et al. (2014) reported an average factor of 4.7 increase of the N_{CCN} during NPF events from growth of new particles to the CCN sizes in Ozark forest. Rose et al. (2017) showed that NPF could be a larger contributor to N_{CCN}

4

91 compared to transport in free troposphere. A long-term field measurement in the urban Vienna

92 conducted by Dameto de España et al. (2017) reported that the N_{CCN} (at 0.5% ss) could increase up to

93 143% during NPF events. Kalkavouras er al. (2017) found that the NPF could double the N_{CCN} (at

94 0.1% ss), but could augment the potential droplet number only by 12%.

95   Factors that control the CCN activity of newly-formed particles (formation rate, growth rate, and

96 particle properties) were investigated worldwide. These parameters varied substantially in a large

97 temporal and spatial scale. For example, the mean formation rate of 10 nm particles (J_{10}) was 3.7 cm^{-3}

98 s^{-1} in Nanjing (An et al., 2015), which was much higher than that (0.40 cm^{-3} s^{-1}) reported in Shanghai

99 (Leng et al., 2014). A value of 3.3~81.4 cm^{-3} s^{-1} was reported for the mean formation rate of 3 nm

100 particles (J_3) based on one-year long measurements in Beijing (Wu et al., 2007). In the NCP region, a

101 long-term measurement conducted by Shen et al. (2011) reported that the J_3 ranged from 0.7 to 72.7

102 cm^{-3} s^{-1}, with a mean value of 8.0 cm^{-3} s^{-1}. Shen et al. (2019) reported an average J_3 value of 1.30 cm^{-3}

103 s^{-1} at Mountain Tai, which was much lower than urban regions. The growth of newly-formed particles

104 can be characterized by the particle growth rates. Kulmala et al. (2004) summarized a wide range of

105 growth rate (1 to 20 nm h^{-1}) from more than 100 filed measurements of NPF in mid-latitudes. On the

106 one hand, the growth rates are usually high in polluted region, for example, a growth rate of 11.6-18.1

107 nm h^{-1} was reported in New Delhi, India (Kulmala et al., 2005;Mönkkönen et al., 2005). On the other

108 hand, the growth rates are in general low in forest regions, for example, a median value of 2.5 nm h^{-1}

109 was reported from long term measurements (Nieminen et al., 2014). Furthermore, large uncertainties

110 exist for the measured growth rates even in the same region. For example, the growth rates under

111 sulfur-poor conditions were about 80% higher than those under sulfur-rich conditions in Beijing (Yue et

112 al., 2011). The condensable vapors not only control the growth rate, but also decide the hygroscopicity

5

113   of newly-formed particle, which can vary in a large range from event to event. Wu et al. (2013)

114   reported a hygroscopic growth factor of 1.2 to 1.55 during NPF events in a mountain region, Germany.

115   Asmi et al. (2010) found a significant contribution of organic vapors to particle formation and growth,

116   leading to a low hygroscopicity of newly-formed particles in the Antarctica region. The above studies

117   show large temporal and spatial variations of characteristics in the properties of newly-formed particles

118   (i.e., the formation rate, growth rate and hygroscopicity) during NPF events. However, how these

119   parameters contribute to the variation of the N_{CCN} during NPF events in various regions is yet to be

120   investigated.

121   Although the Pearl River Delta region (PRD), one of the most economically developed areas in

122   China, has made substantial progress in mitigating haze pollution, especially in achieving $PM_{2.5}$

123   national level II standard (an average annual mass concentration of less than 35 μg m^{-3} for $PM_{2.5}$), the

124   intensive human activities and photochemistry lead to emissions and productions of a large amount of

125   condensable air pollutants for initiating formation of atmospheric particles and promoting their

126   subsequent growth. Several studies have reported the frequent occurrences of NPF events in urban and

127   rural areas of the PRD which provide a large amount of particles to the local atmosphere (Yue et al.,

128   2013;Liu et al., 2008;Yue et al., 2016;Wang et al., 2013). However, these studies focused primarily on

129   the characteristics of the NPF events, the contribution to the N_{CCN} and the controlling factors were still

130   unknown, hindering an accurate assessment of NPF in CCN formation and eventually global climate

131   change.

132   In this study, we analyzed the contribution of NPF to the N_{CCN} based on a rural field campaign

133   conducted at the Heshan supersite in the PRD region during Fall (October and November, 2019). A

134   suite of advanced analytical instruments was employed to measure particle hygroscopicity,

135 size-resolved CCN activity, and particle number size distribution (1 nm - 10 μm). Here, we select three

136 representative NPF events (two from this measurement, the other one from a previous measurement in

137 Panyu, Guangzhou, 2014) to quantitively investigate the contribution of NPF to the N_{CCN} and impact

138 factors (i.e., formation rate, growth rate, background particle concentration, and particle properties) that

139 affect the contribution.

140 **2   Measurement site, instrumentation, and methodology**

141 **2.1 Measurement site**

142   The field campaign was conducted at the Heshan supersite in the Guangdong Province of China

143 during the Fall season (from 27th September to 17th November, 2019). This rural site (22°42′39. 1″N,

144 112°55′35.9″E) is located at the southwest of the PRD region (about 70 km away from megacity

145 Guangzhou) with an altitude of about 40 m above sea-level and the site is surrounded by several farms

146 and villages. All the instruments were placed in an air-conditioned room (T=298K) on the top floor of

147 the building at the supersite, administrated by Guangdong Provincial Environmental Monitoring Centre.

148 Two aerosol sampling ports equipped respectively with a PM$_{10}$ impactor and a PM$_{2.5}$ impactor were

149 made of a 6 m long 3/8″ o.d. stainless-steel tube. The schematic diagram of the inlet system and

150 instrument setup is shown in Fig. S1. The sampling air was dried to a relative humidity (RH) lower

151 than 30% by passing through a Nafion dryer (model MD-700, Perma Pure, Inc., USA) before the air

152 entered into the individual instruments.

2.2 Instrumentation

2.2.1 Particle number size distribution and size-resolved CCN activity measurements

The particle number size distribution (PNSD) in a complete size range of 1 nm- 10 μm (an upper cut size of 10 μm) was measured by a diethylene glycol scanning mobility particle sizer (DEG-SMPS, model 3938E77, TSI Inc., USA), a SMPS (model 3938L75, TSI Inc., USA), and an aerodynamic particle sizer (APS, model 3321, TSI Inc., USA). The DEG-SMPS was applied to measure particles with a size range of 1-30 nm, consisted of a nano-differential mobility analyzer (nDMA, model 3086, TSI Inc., USA), a nano enhancer (model 3777, TSI Inc., USA), and a condensation particle counter (CPC, model 3772, TSI Inc., USA). The SMPS composed of a DMA (model 3081A, TSI Inc., USA) and a CPC (model 3775, TSI Inc., USA) was employed to measure particles in a size range of 10-800 nm. The APS was used to measured submicron particles ranging from 0.5 μm to 10 μm. The data inversion processes for the measured PNSD were done by Aerosol Instrument Manager (version 10, TSI Inc., USA). However, accurate inversion for particles smaller than 3 nm is currently still lacking due to large uncertainties from corrections for multiple charges and diffusion losses. Thus, we only discussed PNSD for particles larger than 3 nm in this study.

Size-resolved CCN activity was measured with a combination of a cloud condensation nuclei counter (CCNc, model 200, DMT Inc., USA) and another SMPS. The CCNc-200 has two parallel cloud columns, which can be used to measure the CCN concentration (N_{CCN}) simultaneously. The supersaturation of each column was set to be 0.1%, 0.2% and, 0.4%, 0.7%, 0.9%, and 1.0%, respectively. The dry particles were firstly neutralized by an X-ray neutralizer (model 3088, TSI Inc., USA) and were then classified by a DMA (model 3081A, TSI Inc., USA). The monodisperse particles

174   were split into three streams: two to the CCNc for measurement of the N_{CCN} (with a flow rate of 0.6

175   LPM) and one to the CPC for measurement of total particle number concentration (N_{CN}, with a flow

176   rate of 0.3 LPM). Prior to the campaign, the SMPSs was calibrated with standard polystyrene latex

177   spheres (PSL, with a size of 20, 50, and 200 nm) and the CCNc-200 was calibrated with ammonium

178   sulfate ((NH_4)$_2$SO$_4$ particles at the six SSs (0.1%, 0.2%, 0.4%, 0.7%, 0.9%, and 1.0%).

179   **2.2.2 Aerosol hygroscopicity measurement**

180   Hygroscopicity of atmospheric particle at various size ranges was measured by a hygroscopic

181   tandem differential mobility analyzer (HTDMA), consisted of two DMA (model 3081L, TSI Inc.,

182   USA), a Nafion humidifier (model MD-700, Perma Pure Inc., USA), a heated tube and a condensation

183   particle counter (model 3788, TSI Inc., USA). The dry particles were firstly neutralizer by an X-ray

184   neutralizer (model 3088, TSI Inc., USA) and subsequently were classified by a DMA for six sizes in

185   this study (30, 50, 80, 100, 150, and 200 nm). The selected particles at a specific diameter (D_0) were

186   then introduced into a humidifier under a fixed RH (90% in this study). Another DMA and a CPC were

187   used to measure size distribution of humified particles (D_{wet}).

188   **2.3 Methodology**

189   **2.3.1 Estimation of hygroscopicity based on the measurements**

190   The size-resolved activation ratio (AR) could be obtained from the measured N_{CN} and N_{CCN} by the

191   SMPS and CCNc-200 system and was inverted based on the method described by Moore et al. (2010).

192   The AR was then fitted with the sigmoidal function with respect to particle diameter D_p,

9

193 $$\frac{N_{CCN}}{N_{CN}} = \frac{B}{1 + (\frac{D_p}{D_{50}})^c}$$ (1)

194 where B, C, and D_{50} are fitting coefficients. The D_{50} represents the critical diameter at which half of

195 the particles are activated at a specific SS.

196 The hygroscopic parameter κ can be obtained from the critical supersaturation (Sc) and the D_{50}

197 (Petters and Kreidenweis, 2007) by

198 $$\kappa = \frac{4A^3}{27D_{50}^3 (\ln Sc)^2} \text{ , where } A = \frac{4\sigma_{s/a} M_w}{RT\rho_w}$$ (2)

199 where $\sigma_{s/a}$ is the surface tension of the solution/air interface and here it is temporarily assumed to be

200 that of pure water (0.0728 N m^{-1} at 298.15 K), M_w is the molecular weight of water (0.018 kg mol^{-1}),

201 R is the universal gas constant (8.31 J mol^{-1} K^{-1}), T is the thermodynamic temperature in Kelvin

202 (298.15 K), and ρ_w is the density of water (about 997.04 kg m^{-3} at 298.15 K).

203 The growth factor (GF) of selected particles can be calculated according to the following equation,

204 $$Gf = \frac{D_{wet}}{D_0}$$ (3)

205 In addition to the hygroscopic parameter calculated based on the SMPS and CCNc-200 system, the κ

206 can also be calculated from HTDMA measurement based on the growth factor,

207 $$\kappa = (Gf^3 - 1) \left[\frac{1}{RH} \exp \left(\frac{4\sigma_{s/a} M_w}{RT\rho_w D_0} - 1 \right) \right]$$ (4)

208 Due to the effect of DMA diffusing transfer function, the TDMAfit algorithm (Stolzenburg and

209 McMurry, 2008) was applied to narrow the uncertainty and fit the growth factor probability density

210 function (GF-PDF). Detailed data inversion process can be found elsewhere in Tan et al. (2013).

211 **2.3.2 Estimation of H$_2$SO$_4$ concentration and its contribution to particle growth**

212 The daytime gas phase H$_2$SO$_4$ concentration is estimated according to the proxy proposed by Lu et

213 al. (2019),

214 $$[H_2SO_4] = 0.0013 \cdot UVB^{0.13} \cdot [SO_2]^{0.40} \cdot CS^{-0.17} \cdot ([O_3]^{0.44} + [NO_x]^{0.41}) \qquad (5)$$

215 where UVB is the ultraviolet radiation B intensity (in W m^{-2}), $[SO_2]$ is the concentration of SO_2 in

216 molecules cm^{-3}, $[O_3]$ is the concentration of O_3 in molecules cm^{-3}, $[NO_x]$ is the concentration of NO_X in

217 molecules cm^{-3}, and the CS is the condensation sink and it can be calculated from following equation,

218 $$CS = 2\pi D \sum_{Dp_i=Dp_{min}}^{+\infty} \beta_m N_i \qquad (6)$$

219 where D is the diffusion coefficient of the H_2SO_4 vapor (assumed to be 0.8×10^{-5} m^2 s^{-1} in this study),

220 $\beta_{m,i}$ is the transitional regime correction factor which can be calculated from the Knudsen number

221 (Fuchs and Sutugin, 1971), and N_i represents the particle number concentration at Dp_i.

222   This proxy is derived based on measurements from a winter field measurement in urban Beijing,

223 where the atmospheric environment is similar to the locations of our measurements. A relative error of

224 about 20% for the proxy proposed by Lu et al. (2019) was estimated based on comparison of the

225 estimated [H_2SO_4] with the measured one. However, accurate quantification of the uncertainty is not

226 feasible since this proxy has not been tested in the PRD region. For simplicity, we adopted a relative

227 error of about 20% for the estimation of sulfuric acid concentration, and ignoring the uncertainties in

228 measuring UVB, [SO_2], CS, [O_3] and [NO_X]. However, further investigation is still needed, since the

229 relative error of the estimation could vary temporally and spatially (Mikkonen et al., 2011).

230   Framework for 0-D Atmospheric Modeling (F0AM) v3.1(Wolfe et al., 2016) is a zero-dimensional

231 atmospheric box model which was used to simulate the concentration of OH radical in the atmosphere.

232 The model was constrained with a set of online measured trace gases, VOCs, and meteorological data.

233 The employed chemical mechanism is Master Chemical Mechanism (MCM) v3.3.1. More detailed

234 description of model setup can be found in Wang et al. (2020).

235   The required vapor concentration of H_2SO_4 ($C_{v,GR=1\,nm\,h^{-1}}$) for a growth rate of 1 nm h^{-1} in a

236   certain particle size range ($D_{p,initial}$ to $D_{p,final}$) can be calculated from the following equation,

237      $$C_{v,GR=1\,nm\,h^{-1}} = \frac{2\rho_v d_v}{\alpha_m m_v \Delta t} \cdot \sqrt{\frac{\pi m_v}{8kT}} \cdot \left[\frac{2x_1+1}{x_1(x_1+1)} - \frac{2x_0+1}{x_0(x_0+1)} + 2ln\left(\frac{x_1(x_0+1)}{x_0(x_1+1)}\right) \right]$$ (8)

238   where ρ_v, m_v and D_v is the density, mass and diameter of H_2SO_4, which was assumed to be 1830 kg

239   m^{-3}, 98 amu, and 0.55 nm, respectively (Nieminen et al., 2010;Jiang et al., 2011), α_m is the mass

240   accommodation coefficient (assumed to be unity in this study), x_1 and x_0 are the ratios of D_v to

241      $D_{p,final}$ (10 nm in this study) and $D_{p,initial}$ (3 nm in this study), Δt (in s) is the time for particle

242   growth from $d_{p,initial}$ to $d_{p,final}$ ($\Delta t = \frac{d_{p,final}-d_{p,initial}}{GR}$) with a growth rate of 1 nm h^{-1}, and k is the

243   Boltzmann constant (1.38×10^{23} J K^{-1}).

244   Thus, the growth rate contributed from condensation of H_2SO_4 vapor can be obtained,

245      $$GR_{H_2SO_4} = \frac{[H_2SO_4]}{C_{v,GR=1\,nm\,h^{-1}}}$$ (9)

246   The average calculated H_2SO_4 concentration during particle growth can be calculated using Eq. (5).

247   The resultant $GR_{H_2SO_4}$ can be overestimated because the assumption of unity for α_m in Eq. (8) is not

248   necessarily the case because not all H_2SO_4 molecules will be captured when colliding with the

249   particles.

250   **2.3.3 Estimation of growth rate (GR) and formation rate (J)**

251   The observed particle growth rate (GR) is defined as the diameter change of nucleated particles

252   (dDp_{nuc}) for a time period (dt),

253      $$GR = \frac{dDp_{nuc}}{dt}$$ (10)

254   Here log-normal distribution function method was adopted and the PNSD was fitted to obtain the

255   representative diameter for nucleated particles during NPF events (Kulmala et al., 2012),

256
$$\frac{dN}{dlogD_p} = \frac{N}{\sqrt{2\pi\sigma}} exp\left(-\frac{ln^2(\frac{Dp}{Dp_{gmd}})}{2\sigma}\right)$$ (11)

257 where D_p is particle diameter, N is total particle number concentration, Dp_{gmd} is geometric mean

258 particle diameter and it was also used as the representative particle size in Eq. (10). In this study, the

259 PNSD was found to have a significant mode in a size range of 3- 60 nm during NPF events and we

260 hence applied one log-normal mode fitting. At each time step, the PNSD was fitted using Eq. (11) and

261 the Dp_{gmd} as a function of time, that is, the growth rate, was determined according to Eq. (10).

262   The formation rate (J_k) described the flux through a certain diameter (k) during NPF events and it

263 is calculated based on the formula given in Cai and Jiang (2017),

264
$$J_k = \frac{dN_{[Dp_k,Dp_u)}}{dt} + \sum_{Dp_g=Dp_k}^{Dp_{u-1}}\sum_{Dp_i=Dp_{min}}^{+\infty}\beta_{(i,g)}N_{[Dp_i,Dp_{i+1})}N_{[Dp_g,Dp_{g+1})} -$$

265
$$\frac{1}{2}\sum_{Dp_g=Dp_{min}}^{Dp_{u-1}}\sum_{Dp_i^3=\max\left(Dp_{min}^3,Dp_k^3-Dp_{min}^3\right)}^{Dp_{i+1}^3+Dp_{g+1}^3\leq Dp_u^3}\beta_{(i,g)}N_{[Dp_i,Dp_{i+1})}N_{[Dp_g,Dp_{g+1})} + n_u \cdot GR_u$$ (12)

266 where $N_{[Dp_k,Dp_u)}$ is particle number concentration in a size range from Dp_k to Dp_u (exclude

267 particles with diameter Dp_u), Dp_k and Dp_u are the lower and upper bound diameters (here 3 and 30

268 nm respectively), $\beta_{(i,g)}$ is the coagulation coefficient for collisions between particles with diameter

269 Dp_i and particles with diameter Dp_g, n_u is the particle distribution function at Dp_u and GR_u is the

270 growth rate calculated using Eq. (10) at Dp_u. Note that the calculation of formation rate using Ep. (12)

271 is based on two assumptions: (1) Dilution and other particles sources and losses except for coagulation

272 loss in the size range from Dp_k to Dp_u are negligible; (2) Net coagulation of particles is negligible.

273 **2.3.4 Measurement based NPF simulations**

274   For a regional NPF event, the evolution of particle size distribution is governed by the population

275 balance equations (Lehtinen et al., 2003; Kuang et al., 2012):

276 $$\frac{dN_{k^*}}{dt} = J_{k^*} - GR \cdot n_{k^*} - N_{k^*} \sum_{Dp_i=Dp_{min}}^{+\infty} \beta_{(k^*,i)} N_i \qquad (13\text{-}1)$$

277 $$\frac{dN_k}{dt} = GR \cdot n_{k-1} - GR \cdot n_k + \frac{1}{2}\sum_{Dp_i=Dp_{min}}^{k-1} \beta_{(i,\varphi)} N_i N_\varphi - N_k \sum_{Dp_i=Dp_{min}}^{+\infty} \beta_{(k,i)} N_i \qquad (13\text{-}2)$$

278 $$Dp_\varphi^3 = Dp_k^3 - Dp_i^3$$

279 (13-3)

280   In the equations, class k^* represents the smallest detectable particle size (here 3 nm particles),

281 J_{k^*} is the formation rate calculated using Eq. (12). Class k represents the particles with diameter Dp_k.

282 The first, second, and third terms on the right-hand side (RHS) of Eq. (13-1) represent the formation,

283 condensation, the coagulation sink terms, respectively. The first and second terms, the third, and fourth

284 terms on the RHS of Eq. (13-2) represent the condensation growth terms, a coagulation source

285 (CoagSrc) term, and the coagulation sink (CoagSnk) term, respectively.

286   For a specific NPF event, the evolution of PNSD with a size range of 3-1000 nm was simulated

287 based on Eq. (13) using Matlab (version 2016a, Mathworks, Inc.). In the simulation, the background

288 particle distribution was assumed to be the average PNSD before 6:00 LT, the growth rate and

289 formation rate were the measured values obtained from Eq. (10) and Eq. (13), respectively, and the

290 time step was set to be 10s. The simulation is based on following assumptions: (1) The dynamics of

291 newly-formed particles are driven by coagulation and condensation. The influences of transportation,

292 primary emissions, dilution, and particle evaporation are negligible. (2) The influence of coagulation on

293 the preexisting particles is negligible. (3) The particle growth rate for all particle sizes is assumed to be

294 the same at a time during NPF events.

3   Results and discussion

3.1 New Particle Formation (NPF) events at the Heshan Site

A total of 20 NPF events were observed during this seven-weeks long field campaign. Here we selected a typical event (29th October, 2019) for further investigation. As shown in Fig. 1a, new particle formation occurred at about 9:50 Local Time (LT) when a significant concentration of 3-10 nm particles were observed. Subsequently, continuous and steady growth of the newly-formed particles was observed until the particles grew to about 70-80 nm at about 20:00 LT. The blue dots in Fig.1a represent the Dp_{gmd} of nucleated particles and the red line represents the linear fitting, leading to an estimated growth rate of 8.0 nm h^{-1}. Prior to the event (around 9:50), the total particle number concentration (N_{CN}) remained low (a concentration slightly below 10000 cm^{-3}) and rapidly increased when NPF event occurred, and then reached its peak (about 56000 cm^{-3}) at 11:15 LT and subsequently decreased to 20000 cm^{-3} at about 15:00 LT, and remained at this concentration for the rest of the day. A steady north wind was observed before 18:00 LT and shifted to northwest afterwards (Fig. 1c). The shift of wind direction led to change of air mass as seen from the PNSD, leading to a sudden increase of the N_{CN} at 18:00 LT (Fig. 1a and b). The CCN concentration (N_{CCN}) at 1.0% SS increased from 5000 cm^{-3} at around 10:00 to 11000 cm^{-3} at about 15:00 LT, when the nucleated particles grew to the CCN size (Fig. S2). The D_{50} at 1.0% SS was apparently the smallest critical diameters among all the SSs, the size that was easily reached during NPF and was significantly affected by the newly-formed particles, we thus only discussed the variation of the N_{CCN} at 1.0% SS in the following section. The sudden increase of N_{CCN} at 18:00 LT could be attributed to change of the air mass due to transportation, consistent with the changes of the PNSD, the N_{CN}, and wind direction (Fig. 1a-c). The activation ratio

316   (AR) was about 0.5 before dawn and dropped to about 0.2 just prior to the event (Fig. 1b). This ratio

317   continued to decrease to its trough at the time corresponding to the maximum of N_{CN} and then

318   increased again to about 0.6 at 15:00 LT during particle growth, slightly higher than the value before

319   dawn. Clearly, NPF can not only add a large number of particles to the atmosphere but also increase the

320   N_{CCN} and AR after particles are formed and grow. The wind speeds were about 3 m s^{-1} during initial

321   formation and growth, and decreased to about 1.5 m s^{-1} during most of the particle growth periods.

322   Formation of gaseous H_2SO_4 was favored by intensive photochemistry. Significant j-values of

323    $O(^1D)$ (in s^{-1}) were observed during the day (from about 7:00 to 17:00) with a maximum value of

324   2×10^{-5} s^{-1} at noon and symmetrically distributed before and after noon. The average calculated H_2SO_4

325   concentration during particle formation periods (10:00-12:00 LT) was about 1.4×10^7 cm^{-3}, about an

326   order higher than that (about 7 - 12×10^6 cm^{-3}) in a mountain region in Germany (Wu et al., 2013) and

327   close to that (about 2-5 $\times$ 10^7 cm^{-3}) in a rural region of Sichuan in China (Chen et al., 2014).

328   Considering a relative error of about 20%, the growth rate contributed by condensation of gaseous

329   H_2SO_4 was about 0.61-1.09 nm h^{-1}, or about 7.6% -13.6% of the observed growth rates for 3-10 nm

330   particles. It should be pointed out that the above estimates for the growth rates are subject to large

331   uncertainties due to uncertainties for the estimation of sulfuric acid concentration using Eq. (5) as the

332   proxy and here a unity of sticking coefficients was assumed when gaseous H_2SO_4 molecules collide

333   with pre-existing particles. This implies that other compounds (e.g., organic vapors) than H_2SO_4 play

334   significant roles in the growth process of newly-formed particles which was widely reported in

335   literatures (Boy et al., 2005;Casquero-Vera et al., 2020;Paasonen et al., 2010).

3.2 The impact of hygroscopicity and surfactants on N_{CCN}

The ability that atmospheric particles can serve as CCN is determined by several factors including sizes, chemical composition, surface tension, and water saturation ratio of the particles (Farmer et al., 2015). The organic matter in particles can act as surfactants to lower the surface tension of the particles and hence can increase the CCN activity (Ovadnevaite et al., 2017). Previous studies showed that surfactants could modify the ability of water uptake, leading to discrepancies of κ values between measurements using techniques under different water saturation conditions, e.g., sub-saturation (HTDMA measurements) or supersaturation (CCNc measurements) (Cai et al., 2018; Wex et al., 2009; Rastak et al., 2017; Ruehl and Wilson, 2014). Figure 2 compares the κ values measured from several locations including Heshan (this study, rural), Panyu (urban PRD, Cai et al., 2018), North China Plain (Liu et al., 2011), and South China Sea (Cai et al., 2020). The median κ values measured by HTDMA in this study ranged from 0.1 to 0.18 in a size range of 30-200 nm, similar to those of particles primarily composed of organics (Deng et al., 2019; Liu et al., 2018; Pajunoja et al., 2015), implying that chemical composition of the measured particles was dominated by organics. In particular, the κ values measured using HTDMA (κ_{HTDMA}) in this study were significantly lower than those from other studies. The κ values in a range of 0.21-0.31 were reported for urban PRD and suburban North China Plain, which were likely attributed to high fractions of water-soluble organic matters and inorganic compounds from traffic and industry emissions. The κ values measured using CCNc (κ_{CCN}) fall in a range from 0.19 to 0.46, much higher than those from measurements using HTDMA in this study. The discrepancy of the κ κ_{HTDMA} and κ_{CCN} values suggests that surfactant effects could play an important role in CCN activation under sub-saturation and supersaturation environments. Previous studies have

shown that the organics in particles could lower surface tension by about 0.01-0.032 N m^{-1}

(Ovadnevaite et al., 2017; Liu et al., 2018; Engelhart et al., 2008; Cai et al., 2018), leading to the

decrease of the D$_{50}$ and higher κ values. This effect was closely related to the presence of liquid-liquid

phase separation (LLPS) (Renbaum-Wolff et al., 2016), which was observed in organic-containing

particles under high relative humidity. LLPS is mainly depended on the chemical composition of

organics (e.g., functional groups and oxidation state) and inorganic-organic mixing ratio (Ruehl et al.,

2016; Ma et al., 2021; Bertram et al., 2011). Once LLPS occurred, organic-rich phase on the droplet

surface would reduce surface tension and further enhance water uptake (Rastak et al., 2017;Freedman,

2017). Surface tension is expected to increase with droplet growth, since the organic-rich phase

becomes thinner and shifted to water-rich phase (Liu et al., 2018; Renbaum-Wolff et al., 2016;

Ovadnevaite et al., 2017). Further laboratory and field studies are needed for better understanding the

occurrence of LLPS in particles, its variation with different chemical composition, and its impact on

the surface tension.

A surface tension value ($\sigma_{s/a}$*=0.060 N m^{-1}) was adopted to calculate both the κ$_{CCN}$ (denoted as

κ$_{CCN}$ $\sigma_{s/a}$*) and κ$_{HTDMA}$ (κ$_{HTDMA}$ $\sigma_{s/a}$*) using Eq. (2) and Eq. (4), respectively. No significant changes of κ

values (i.e., from 0.11 to 0.10 for 30 nm particles) were found from TDMA measurements (Fig. S3),

while the κ values from CCNc measurements using this surface tension value ($\sigma_{s/a}$*) were still lower

than those using pure water assumption and the differences became larger with increasing particle sizes,

implying that the surface tension is dependent on particle diameter. It also implies that the κ value was

more susceptible to surfactants under supersaturation condition, which can lower the D$_{50}$ of the particle

for facilitating CCN activation. For particles with the same κ value, the measured D$_{50}$ (denoted as D$_{50,m}$)

by fitting of N$_{CCN}$/N$_{CN}$ using Eq. (1) was lower than the calculated value based on pure water surface

379   tension using Eq. (2) due to the surfactant effect. In order to estimate the impact of surfactant on

380   particle activation, the D_{50} was recalculated using the surface tension of pure water (0.072 N m^{-1}) by Eq.

381   (2) based on the κ value from the CCN measurements with a surface tension correction (refer to κ_{CCN}

382    $\sigma_{s/a}{}^{*}$ and $\sigma_{s/a}{}^{*}$=0.060 N m^{-1} in Fig. 2). We termed the above recalculated D_{50} as the $D_{50,r}$ to illustrate the

383   surfactant effects on the CCN activity during NPF events. Figure 3 shows the variation of the $D_{50,r}$

384   (here $\sigma_{s/a}$=0.072 N m^{-1}) and the $D_{50,m}$, along with the Dp_{gmd} of the nucleated particles during the NPF

385   event. The $D_{50,m}$ was lower than the $D_{50,r}$ by about 10 nm. As a result, the Dp_{gmd} reached the $D_{50,m}$ at

386   about 15:00 LT, about two hours earlier than it arrived at the $D_{50,r}$, which indicates that the surfactant

387   effects could lead to earlier activation of the newly-formed particles as CCN. The earlier the Dp_{gmd}

388   reaches the critical diameter D_{50}, the higher the N_{CCN} is because more particles can survive from being

389   scavenged by preexisting particles. The difference of PNSD at the time when the Dp_{gmd} reached

390   respectively the $D_{50,m}$ and the $D_{50,r}$ is shown in Fig. S2. The peak value of PNSD at 15:00 LT was about

391   20000 cm^{-3} higher than the value at 17:15 LT. The N_{CCN} also shows a difference between the $D_{50,r}$ and

392    $D_{50,m}$ (Fig. 4a).

393   We also investigate the effect of the surface tension on the N_{CCN} at SS=1.0% by varying the value

394   of the surface tension. As we mentioned in the beginning of this section, a surface tension of 0.060 N

395   m^{-1} ($\sigma_{s/a}{}^{*}$) was adopted when discussing the CCN activation at 1.0% SS and we assume that the $D_{50,r}$

396   was based on this surface tension value. The average D_{50} (denoted as $D_{50,a}$) was the mean of the $D_{50,m}$.

397   The N_{CCN} is calculated by integrating particle concentrations above D_{50} using the following equation,

398        $$N_{CCN} = \int_{D_{50}}^{\infty} n_i d log D p_i \qquad\qquad (14)$$

399   where n_i is the particle distribution function at Dp_i. The D_{50} can be the measured or recalculated one.

400   It was shown that the N_{CCN} at SS=1.0% from integration of particles above the $D_{50,r}$ was significantly

401   lower than that above the $D_{50,m}$ after 12:00 LT (two hours after the occurrence of the NPF event), with

402   concentration differences of about 3000-4000 cm^{-3} (Fig. 4a). The AR based on the $D_{50,r}$ reached its

403   minimal values between 10:00 and 12:00 LT, and then steadily increased until 22:00 and subsequently

404   decreased. The AR based on the $D_{50,m}$ reached its minimal during the same period as the AR from the

405   $D_{50,r}$; however, it then rapidly increased until 16:00 and the continuing increase of the AR was much

406   slower until 22:00, and also subsequently decrease for the last hour of the measurement (Fig. 4b). This

407   different trend was likely attributed to the continuing growth of the nucleated particles to the CCN size

408   prior to 16:00. Here, we define the deviation of N_{CCN} based on the $D_{50,r}$ from that based on the $D_{50,m}$ to

409   evaluate the impacts of the surface tension (primarily due to the surfactant effects) on the N_{CCN},

410   $$\delta_{N_{CCN}} = \frac{N_{CCN,m} - N_{CCN,r(or\ a)}}{N_{CCN,m}} \qquad (15)$$

411   where the $N_{CCN,m}, N_{CCN,r}$ represent the N_{CCN} based on the $D_{50,m}$ and the $D_{50,r}$ or $D_{50,a}$. The $\delta_{N_{CCN}}$ of

412   the $D_{50,r}$ was about 0.1 prior to the NPF event, and reached a peak value of 0.4 at 14:00 LT, and then

413   decreased steadily to 0.1 at 22:00 and remained unchanged for the last hour of the measurement (Fig.

414   4c). The results suggests that the decrease of the surface tension due to the surfactant effects could lead

415   to about 10% increase of the N_{CCN} at 1.0% SS for non-event period and about 40% increase during the

416   NPF event (Fig. 4c). Apparently, the surfactants have more significant effects on N_{CCN} during the NPF

417   event period than during non-event period, as the difference between the $\delta_{N_{CCN}}$ based on the $D_{50,r}$ and

418   the $D_{50,a}$ was significant only during the event period (12:00-18:00 LT).

419   The hygroscopicity of newly-grown particles can have significant impact on the N_{CCN} during the

420   NPF event. During the campaign, the minimum particle size of CCN activity measurement was about

421   40-45 nm (at 1.0% SS), thus the hygroscopicity of this size range was used to present the property of

422   the newly-grown particles, when they grow up to this size range. In general, the κ_{CCN} values for 40-45

nm particles were significantly higher (corresponding to much higher hygroscopicity) during early

event period than during non-event and other event periods (Fig. S4a). Hence, we adopted a minimum

size range of 40-45 nm particles for CCN activity measurements (at about 1.0% SS) to represent

typically growth of newly-formed particles to this size range during the campaign. It should be pointed

out that the high κ values during 10:00~12:00 LT did not represent the hygroscopicity of the

newly-grown particles which were primarily composed of particles much smaller than 30-40 nm. Those

new particles grew to about 40-50 nm at 14:00-16:00 (Fig. 1a and Fig. 3) and their κ values were

obviously lower than the average ones, implying that the organic vapors could play an important role

during growth of new particles as discussed in Section 3.1. The decrease of hygroscopicity due to

condensation of organic vapors can lead to an increase of about 3-4 nm for the D_{50}, much smaller than

the increase of about 10 nm induced by the surfactant effect which reduces the surface tension as

discussed before. The results indicate that the surfactant effect may play a more important role than

hygroscopicity in the N_{CCN} because the surfactant effect can largely decrease the D_{50} during the NPF

event when the number concentration of particles is dominant by Aitken mode.

3.3 The impact of the dynamic processes on N_{CCN}

As discussed in section 2.3.4, the dynamical processes for new particles during nucleation events

are governed by the population balance equation (Eq. (13)). Here, we build a MATLAB program to

model the NPF event using Eq. 13, with input parameters including background particle distribution,

growth rate and formation rate. Notice that the simulation is based on the aforementioned three

assumptions. Figure 5 shows the measured and modeled PNSD, N_{CN}, and N_{CCN} at 1.0% SS. To be

simplified, the background particle distribution was assumed to be the average particle distribution

444 before 6:00 LT. The modeled PNSD and N_{CN} agree very well with the measured ones, except the model

445 fail to reproduce the abrupt change of PNSD and N_{CN} between 18:00 and 22:00. As discussed in section

446 3.1, this discrepancy was attributed to the change of the air mass by wind direction which was not

447 considered in the model. However, there are considerable discrepancies between the modeled and the

448 measured N_{CCN}. The measured N_{CCN} at 1.0% SS increased steadily after the occurrence of the NPF

449 event (at around 9:00 LT) due to formation of high concentration particles at a size range of 10-60 nm

450 until around 19:00 and subsequently the N_{CCN} dropped for the rest of the day. The model N_{CCN} started

451 to increase at about 14:15 LT and reached its maximum level at about 17:00 LT. The model failed to

452 reproduce the increase of the measured N_{CCN} before 16:00, although the reasons corresponding to the

453 discrepancy are still unknown. The modeled peak value of the N_{CCN} at 1.0% SS was about 12000 cm^{-3},

454 which agreed very well with the measured one (11000 cm^{-3}). Again, the model failed to reproduce the

455 increase of N_{CCN} due to the change of the air mass between 18:00 and 22:00.

456   As discussed in section 3.2, the contribution of N_{CCN} was affected by the properties of

457 newly-grown particles. However, the characteristics of NPF, including growth rate, formation rate and

458 the background PNSD also affect N_{CCN}. The effects of variation (halving or doubling) of the growth

459 rate, formation rate, and the background PNSD on the N_{CN} and N_{CCN} were investigated to test the

460 sensitivity of those parameters. Figure 6 shows the comparison of the measured N_{CN} and N_{CCN} with

461 their respective modeled values based on the half or doubling of each tested parameter, respectively. As

462 can be seen from Fig. 6a, the modeled N_{CN} values based on the double GR, the double formation rate

463 and the half background PNSD were higher than the corresponding measured values, respectively, and

464 vice versa. Doubling of the formation rate lead to formation of more new particles and the half

465 background PNSD corresponds to a low coagulation loss with pre-existing particles, resulting in

22

466 production of more new particles in the simulation. Doubling of the GR resulted in a higher

467 concentration of particles, probably due to the significant increases of the coagulation source (Fig. S5b),

468 while small decreases for both of the coagulation sink and growth term were found (Fig. S5a and Fig.

469 S5d). Coagulation source means that two smaller particles collide with each other and become a larger

470 particle, which can also increase the population of new particles. Since the newly-formed particles can

471 grow to larger sizes under a higher GR, the PNSD of new particles would be broader (Fig. S6), which

472 provides a wider "region" for the coagulation sources, i.e. the "$k-1$" in eq. (13-2) is higher. Doubling

473 of the FR (J) resulted in the highest modeled N_{CN} (about 90000 cm^{-3}) among all simulated cases;

474 however, the modeled N_{CCN} based on a double J was only the second highest value (about 15000 cm^{-3}).

475 The highest modeled N_{CCN} (about 25000 cm^{-3}) was found to double the GR and moreover it peaked

476 earlier at about 14:00 LT (two hours earlier than the other cases). Similarly, the highest modeled AR

477 (about 0.82) was from doubling the GR and an earlier peak time was also found (Fig. S7). The above

478 results can be attributed to the following two possible reasons: (1) Doubling of the GR made

479 newly-formed particles grow faster to the D_{50} which facilitated the survival of more particles from

480 coagulation scavenging; (2) The N_{CN} became higher by doubling the GR. If newly-formed particle

481 grew slowly, for example, the decrease of the GR to a half value would result in growth of most

482 particles to diameters below that of the D_{50}, leading to the smallest change of the N_{CCN} compared to

483 other cases (Fig. S7). The pre-existing background particles can serve as the coagulation sinks for

484 newly-formed particles and hence can prevent them from growing to the CCN sizes. For example,

485 under the double background PNSD condition, the N_{CN} reached its peak of about 38000 cm^{-3} at about

486 11:00 and quickly dropped afterward. The newly-formed particles contributed about 3000 cm^{-3} to the

487 N_{CCN}, or an AR of about 0.45 at about 17:30 LT, an insignificant change compared to the value for the

488 non-event period, implying that under a high background particle concentration, NPF events have a

489 minor contribution to the N_{CCN}. Doubling or halving of the FR resulted respectively in contribution of

490 about 11000 and 5000 cm^{-3} to the N_{CCN}; however, the magnitude of contribution from variation of the

491 FR was relatively lower than that from the GR and the background PNSD.

492   Figure 7 shows the comparison of the itemized absolute and fractional contribution of coagulation

493 sink, coagulation source, GR and J to the N_{CCN} for the above several scenarios (model, double GR, half

494 or double J, and half or double PNSD). Here, the individual contribution was integrated from the

495 corresponding term in Eq. (13) for all particle sizes from the initial time of the NPF event to the time

496 when the N_{CCN} reached the peak concentration. As clearly shown in Fig. 7, the coagulation source term

497 plays an more important role in the N_{CCN} (with a fraction of about 13%) for the double GR case than

498 any other cases. As discussed above, doubling of FR (J) and halving of PNSD led to similar N_{CCN} peak

499 values (about 15000 and 13500 cm^{-3}, respectively); however, the dynamics processes for the two

500 scenarios were significantly different. For the double J case, the formation term contributed about

501 240000 cm^{-3} to the N_{CCN}, much higher than the half PNSD case, and the CoagSnk and CoagSrc terms

502 were much higher (about -260000 and 50000 cm^{-3}, respectively) than any other cases due to formation

503 of high concentration of newly-formed particles. Moreover, under the double J scenario, the fraction of

504 CoagSnk term was higher, while the CoagSrc term was lower than the half PNSD case, indicating a

505 more significant coagulation scavenging with preexisting particles. As a result, the N_{CN} quickly

506 dropped from its peak value to a concentration level similar to the half PNSD case within one hour (Fig.

507 6a). Based on the above reasons, the contribution of the newly-formed particles to the N_{CCN} was

508 relatively smaller for the double J case than the double GR or half PNSD cases, although its

509 coagulation source term and J term were the highest among all the cases.

510   To compare different impacts of the characteristics and properties of newly-formed particles, the

511   N_{CCN} was simulated through varying parameters of different characteristics (case 1, 4 and 7) and

512   properties (case 2, 3, 5, 6, 8 and 9). The input parameters for different cases are shown in Table S1. For

513   case 2, 3, 5, 6, 8 and 9 scenarios, the surface tension or hygroscopicity was adjusted to match similar

514   N_{CCN} values based on different NPF characteristics (case 1, 4 and 7, respectively). The results show that

515   doubling GR produces the most significant impact on the N_{CCN}, and the surface tension (κ value) was

516   adjusted to 0.030 N m^{-1}(1.2) to have the same impact (Fig. 8a). Obviously, a κ value of 1.2 for

517   hygroscopicity is much higher than that of many inorganics, e.g., H_2SO_4 (κ=0.90, Topping et al., 2005)

518   and NH_4NO_3 (0.58, Topping et al., 2005). Meanwhile, the surface tension was lower than the values

519   (0.049-0.060) reported previously (Ovadnevaite et al., 2017; Engelhart et al., 2008; Cai et al., 2018).

520   However, doubling GR value (16.0 nm h^{-1}) was reasonable and consistent with previous studies

521   (Mönkkönen et al., 2005; Foucart et al., 2018; O'Dowd et al., 1999), suggesting significant contribution

522   of GR to the growth. For doubling formation rate and halving PNSD, the modified surface tension and

523   κ values were minor (Fig. 8b and c).

524   **3.4 Modeling of the impact factors on the N_{CCN} during NPF events**

525   Here we include two more NPF events to investigate the influence of several important impact

526   factors (growth rate, formation rate, and background particles) on the N_{CCN}, one from this campaign

527   (October 18th, 2019), another from the field campaign in Panyu (December 12th, 2014). Both

528   campaigns were conducted in the PRD region, details of the field campaign in Panyu can be found in

529   Cai et al. (2018). We applied the same model to simulate NPF as discussed in the previous section.

530   Figure 9 shows the measured (a), modeled (b) PNSD, along with the N_{CN} (c). For a better comparison

531   among all the cases, all the modeled PNSDs were based on the measured formation rate (J_{10}) due to

532   lack of measurement data for particles below 10 nm in the Panyu campaign. The background particle

533   distributions were assumed to be the average values before 7:00 LT. In addition, since no measurement

534   data were available for the CCN activity at 1.0% SS during the Panyu campaign, the N_{CCN} for this

535   campaign was calculated from the average CCN activation curve at 1.0% SS in the two Heshan events

536   and the PNSD of the Panyu event using following equation,

537     $$N_{CCN} = \int_{Dp_i=Dp_{min}}^{\infty} AR_i n_i dlogDp_i \tag{16}$$

538   where the AR_i is the average activation ratio (in Heshan) at Dp_i and the n_i is the particle

539   distribution function (in Panyu) at Dp_i.

540   In general, the modeled PNSDs agreed well with the measured ones for the NPF events under

541   investigation (Fig. 9a-f). The N_{CN} values were excellently predicted during the initial particle formation

542   period before the maximum values were reached (Fig. 9g-i). In particular, the N_{CN} was well predicted

543   for the study case (the October 29 event) except for the period when the air mass changed as has been

544   discussed in the previous section. For the October 18 event, however, the model underpredicted the

545   N_{CN} shortly after it reached the peak value which can be attributed to significant variation of Aitken

546   mode during the event. For example, the model failed to reproduce concentration trend of 10-60 nm

547   particle at the early event stage (Fig. 10a-b). For the December 12 event, the model underpredicted a

548   significantly lower peak concentration (about 4100 cm^{-3} lower) at about 12:00 pm than the measured

549   one, due probably to presence of a significant amount of larger background particles (100-200 nm)

550   which were not taken into account in the model (Fig. 9c and Fig. 10c). As a result, the N_{CCN} was

551   underpredicted in two Heshan events (fig. 10a- b), owing to the fluctuation of background particle

552   distribution and unexplained increase of concentration of particles at a size range of 10-60 nm at the

26

553   beginning of event. While for the Panyu event (the December 12 event), a significant underestimate

554   (about 4100 cm^{-3} lower than the measured N_{CN}) for the peak concentration was made at about 12:00 pm,

555   due probably to the presence of a significant amount of other bigger background particles (100-200 nm)

556   after 12:00 pm which was not able to be taken into account in the model (Fig. 9c). Thus, the predicted

557   N_{CCN} value was substantially lower than the measured one for the December 12 event (Fig. 10c). This

558   also indicates that the N_{CCN} was primarily contributed from the background preexisting particles rather

559   than newly-formed particles form the NPF event in the December 12 event case. The maximum

560   modeled peak N_{CCN} value (about 7000 cm^{-3}) is significantly lower that of the other two events (about

561   15000 and 12000 cm^{-3}, respectively), which could be attributed to the lower growth rates, formation

562   rate, and the high CS value (Fig. S8 for J_{10} and table S2 for GR and CS). We further simulate the

563   December 12 event to investigate the most important impact factor that influences the N_{CCN} using

564   different characteristics from the two other NPF events (Fig. 11), including the growth rate on the

565   October 18 event (high growth rate scenario), the formation rate on the October 29 event (high

566   formation rate scenario), and the background PNSD on the October 29 event (mainly distributed in

567   Aitken mode, denoted as low CS PNSD scenario). The results show that all the new modeled N_{CN} value

568   were higher than the initial modeled N_{CN} value. The N_{CN} was significantly increased and earlier peaked

569   (with a peak value about 38000 cm^{-3}) under the high formation rate scenario, while the N_{CCN} was

570   mainly affected and also earlier peaked under the high growth rate scenario. The peak value of N_{CCN}

571   increased from 6000 cm^{-3} to 14000 cm^{-3} and the peak time varied from 20:00 LT to 16:00 LT. The N_{CN}

572   value increased under the low CS PNSD scenario; however, the N_{CCN} barely changed, implying that

573   larger size particles in the preexisting background play a more important role in scavenging

574   newly-formed particles. We hence conclude that the newly-formed particles with a higher growth rate

575   would grow faster to the CCN size by avoiding higher number concentration losses in the atmosphere

576   (Fig. S9a). Our results highlight the importance of particle growth rate in modulating the N_{CCN} during

577   NPF events.

578   It should be noted that the three NPF events discussed in this study were generally "Class I"

579   regional NPF events, for which the growth rate and formation rate could be obtained with high

580   confidence (Dal Maso et al., 2005). Other types (i.e., Class II proposed by Dal Maso et al. (2005)) were

581   not considered since their growth rates and formation rates are extremely difficult to be determined,

582   leading to high uncertainties in model simulation of these events. In addition, we did not include the

583   "transport" type of NPF events, for which new particles were formed somewhere else and then

584   transported to the measurement site, because the model ignores the impact of transport. Some events

585   belonging to "Class II" type and "transport" type were observed during the campaign (Fig. S10). For

586   the "Class II" type (Fig. S9 a), the number concentration and diameter of the nucleation and Aitken

587   mode particles vary significantly. For the "transport" type (Fig. S10 b), the concentration of 3-30 nm

588   particles at 10:00-12:00 LT was much lower than that of 30-70 nm at 12:00-20:00 LT, indicating the

589   impact of transport. Investigation on the contribution of other NPF types to the N_{CCN} is needed in future

590   studies. Moreover, this study only analyzed three NPF events as representatives of Class I type in the

591   PRD region, and more field campaigns in other regions and seasons are also needed to identify the

592   major impact factor.

593   **4   Conclusions**

594   Field measurements were conducted at a rural site in the PRD region of China during October and

595   November 2019. The contribution of new particle formation (NPF) to the N_{CCN} was investigated based

on three chosen NPF events including two (29th October and 18th November, 2019) from this field campaign and one (12th December, 2014) from a previous campaign in Panyu. The effects of several controlling factors on the contribution were explored to better understand the CCN activation process. These factors include formation rate, growth rate, background particle distribution, hygroscopicity and surface tension of the particles. Significant discrepancies were found for the κ values between measurements under supersaturation (using CCNc) and those under sub-saturation (using HTDMA), due partly to the pure water assumption for the surface tension when calculating the κ values based on the CCNc measurements. Organics in the particles could act as surfactants to lower the surface tension which facilitate CCN activation during NPF events. The results show that a surface tension value of about 0.060 N m^{-1} instead of 0.073 N m^{-1} (pure water assumption) could decrease the D_{50} (SS=1.0%) for 10 nm particles, bringing the agreement of the κ values between CCNc and HTDMA measurements. The surfactant effects caused by organics in the particles would increase the N_{CCN} at SS=1.0% by about 20% during non-event periods and by about 40% during NPF events. In addition, an earlier peak time was also observed because much higher number concentrations of small particles (3-100 nm) during the event would lead to smaller D_{50}.

The dynamic population balance equations were employed to qualitatively simulate NPF events under different case scenarios (coagulation term, formation term and growth term). Sensitivity studies were then performed to analyze the contribution of each aforementioned term to the N_{CCN}. The results show that high formation rates, high growth rates, and low background particle concentrations lead to high total and CCN concentrations, although different mechanisms were attributed to the high N_{CN} and N_{CCN}. High formation rates lead to high particle production in the atmosphere; likewise, high growth rates produce a broad distribution of new particles and further increase the coagulation sources, while

618 low background concentrations result in low coagulation scavenging with preexisting particles. Among

619 these controlling factors, the growth rate was found to have the most significant impact on the N_{CCN},

620 because a faster growth for newly-formed particles resulted in growing these particles to the CCN sizes

621 in a shorter time before they were scavenged by preexisting particles. The N_{CCN} (SS=1.0%) measured

622 from the chosen event on 12th December, 2014 was significantly lower than that from two other chosen

623 events, initially attributed to the low growth rate, low formation rate, and low background particle

624 concentration. Sensitivity tests were then performed under different scenarios (the highest growth rate

625 form the event on 18th October, the highest formation rate and the lowest CS from the event on 29th

626 October, respectively) with change of only one factor for each simulation. The results show that the

627 peak value of the modeled N_{CCN} increased from 6000 to 14000 cm^{-3} with the new applied growth rate,

628 leading to a similar value to that from the event on 18th October, while the modeled N_{CCN} values were

629 barely affected under the two other scenarios. These results highlight the importance of the growth rate

630 in the contribution of the controlling factors to the N_{CCN}. We concluded that surface tension and growth

631 rate played a major role in the contribution of NPF event to the N_{CCN}. More work on the other NPF

632 cases is obviously needed in order to better understand the contribution to the N_{CCN} and its impact on

633 climate.

634

635 *Data availability.* Data from the measurements are available upon request (Bin Yuan via

636 byuan@jnu.edu.cn).

637

638 *Supplement.* The supplement related to this article is available online at xxx.

639

640 *Author contributions.* **MC, MS** and **BY** designed the research. **MC, MS, BY**, **SH, YP, ZW, DC, BL**

641 **and QS** performed the measurements. **MC, BY, JZ, HT, FL, SH, HX, LL, YP, ZW, BL and QS**

642 analyzed the data. **MC, BY** and **JZ** wrote the paper with contributions from all co-authors.

643

644 *Competing interests.* The authors declare that they have no conflict of interest.

645

654

655 **Reference**

656   An, J., Wang, H., Shen, L., Zhu, B., Zou, J., Gao, J., and Kang, H.: Characteristics of new particle

657 formation events in Nanjing, China: Effect of water-soluble ions, Atmos. Environ., 108, 32-40,

658 https://doi.org/10.1016/j.atmosenv.2015.01.038, 2015.

659   Asmi, E., Frey, A., Virkkula, A., Ehn, M., Manninen, H., Timonen, H., Tolonen-Kivimäki, O.,

660 Aurela, M., Hillamo, R., and Kulmala, M.: Hygroscopicity and chemical composition of Antarctic

661 sub-micrometre aerosol particles and observations of new particle formation, Atmos. Chem. Phys., 10,

662 4253-4271, 2010.

663   Bertram, A. K., Martin, S. T., Hanna, S. J., Smith, M. L., Bodsworth, A., Chen, Q., Kuwata, M.,

664 Liu, A., You, Y., and Zorn, S. R.: Predicting the relative humidities of liquid-liquid phase separation,

665 efflorescence, and deliquescence of mixed particles of ammonium sulfate, organic material, and water

666 using the organic-to-sulfate mass ratio of the particle and the oxygen-to-carbon elemental ratio of the

667 organic component, Atmos. Chem. Phys., 11, 10995-11006, 10.5194/acp-11-10995-2011, 2011.

668   Boy, M., Kulmala, M., Ruuskanen, T. M., Pihlatie, M., Reissell, A., Aalto, P. P., Keronen, P., Dal

669 Maso, M., Hellen, H., Hakola, H., Jansson, R., Hanke, M., and Arnold, F.: Sulphuric acid closure and

670 contribution to nucleation mode particle growth, Atmos. Chem. Phys., 5, 863-878,

671 10.5194/acp-5-863-2005, 2005.

672   Cai, R., and Jiang, J.: A new balance formula to estimate new particle formation rate: reevaluating

673 the effect of coagulation scavenging, Atmos. Chem. Phys., 17, 12659-12675,

674 10.5194/acp-17-12659-2017, 2017.

675   Cai, M., Tan, H., Chan, C. K., Qin, Y., Xu, H., Li, F., Schurman, M. I., Liu, L., and Zhao, J.: The

676 size-resolved cloud condensation nuclei (CCN) activity and its prediction based on aerosol

677 hygroscopicity and composition in the Pearl Delta River (PRD) region during wintertime 2014, Atmos.

678 Chem. Phys., 18, 16419-16437, 2018.

679   Cai, M., Liang, B., Sun, Q., Zhou, S., Chen, X., Yuan, B., Shao, M., Tan, H., and Zhao, J.: Effects

680 of continental emissions on cloud condensation nuclei (CCN) activity in the northern South China Sea

681 during summertime 2018, Atmos. Chem. Phys., 20, 9153-9167, 10.5194/acp-20-9153-2020, 2020.

682   Casquero-Vera, J. A., Lyamani, H., Dada, L., Hakala, S., Paasonen, P., Román, R., Fraile, R.,

Petäjä, T., Olmo-Reyes, F. J., and Alados-Arboledas, L.: New particle formation at urban and high-altitude remote sites in the south-eastern Iberian Peninsula, Atmos. Chem. Phys. Discuss., 2020, 1-32, 10.5194/acp-2020-394, 2020.

Chen, C., Hu, M., Wu, Z., Wu, Y., Guo, S., Chen, W., Luo, B., Zhang, Y., and Xie, S.: Characterization of new particle formation event in the rural site of Sichuan Basin and its contribution to cloud condensation nuclei, China Environ. Sci., 34, 2764-2772, 2014. (in Chinese)

Dal Maso, M., Kulmala, M., Riipinen, I., Wagner, R., Hussein, T., Aalto, P. P., and Lehtinen, K. E. J.: Formation and growth of fresh atmospheric aerosols: eight years of aerosol size distribution data from SMEAR II, Hyytiälä, Finland, Boreal Environ. Res., 10, 323-336, 2005.

Dameto de España, C., Wonaschütz, A., Steiner, G., Rosati, B., Demattio, A., Schuh, H., and Hitzenberger, R.: Long-term quantitative field study of New Particle Formation (NPF) events as a source of Cloud Condensation Nuclei (CCN) in the urban background of Vienna, Atmos. Environ., 164, 289-298, https://doi.org/10.1016/j.atmosenv.2017.06.001, 2017.

Deng, Y., Yai, H., Fujinari, H., Kawana, K., Nakayama, T., and Mochida, M.: Diurnal variation and size dependence of the hygroscopicity of organic aerosol at a forest site in Wakayama, Japan: their relationship to CCN concentrations, Atmos. Chem. Phys., 19, 5889-5903, 10.5194/acp-19-5889-2019, 2019.

Engelhart, G., Asa-Awuku, A., Nenes, A., and Pandis, S.: CCN activity and droplet growth kinetics of fresh and aged monoterpene secondary organic aerosol, Atmos. Chem. Phys., 8, 3937-3949, 2008.

Farmer, D. K., Cappa, C. D., and Kreidenweis, S. M.: Atmospheric Processes and Their Controlling Influence on Cloud Condensation Nuclei Activity, Chemical Reviews, 115, 4199, 2015.

Freedman, M. A.: Phase separation in organic aerosol, Chem. Soc. Rev., 46, 7694-7705, 10.1039/C6CS00783J, 2017.

Foucart, B., Sellegri, K., Tulet, P., Rose, C., Metzger, J. M., and Picard, D.: High occurrence of new particle formation events at the Maïdo high-altitude observatory (2150 m), Réunion (Indian Ocean), Atmos. Chem. Phys., 18, 9243-9261, 10.5194/acp-18-9243-2018, 2018.

Fuchs, N., and Sutugin, A.: High Dispersed Aerosols, Topics in Current Aerosol Research, in: International Reviews in Aerosol Physics and Chemistry, Pergamon Press Oxford, 5-60, 1971.

712   Jiang, J., Zhao, J., Chen, M., Eisele, F. L., Scheckman, J., Williams, B. J., Kuang, C., and

713   McMurry, P. H.: First Measurements of Neutral Atmospheric Cluster and 1–2 nm Particle Number Size

714   Distributions During Nucleation Events, Aerosol Sci. Technol., 45, ii-v,

715   10.1080/02786826.2010.546817, 2011.

716   Kalkavouras, P., E. Bossioli, S. Bezantakos, A. Bougiatioti, N. Kalivitis, I. Stavroulas, G.

717   Kouvarakis, A. P. Protonotariou, A. Dandou, G. Biskos, N. Mihalopoulos, A. Nenes, & M. Tombrou

718   (2017), New particle formation in the southern Aegean Sea during the Etesians: importance for CCN

719   production and cloud droplet number, Atmos. Chem. Phys., 17(1), 175-192,

720   doi:10.5194/acp-17-175-2017.

721   Kuang, C., Chen, M., Zhao, J., Smith, J., McMurry, P. H., and Wang, J.: Size and time-resolved

722   growth rate measurements of 1 to 5 nm freshly formed atmospheric nuclei, Atmos. Chem. Phys., 12,

723   3573-3589, 10.5194/acp-12-3573-2012, 2012.

724   Kulmala, M., Vehkamäki, H., Petäjä, T., Dal Maso, M., Lauri, A., Kerminen, V. M., Birmili, W.,

725   and McMurry, P. H.: Formation and growth rates of ultrafine atmospheric particles: a review of

726   observations, J. Aerosol Sci., 35, 143-176, https://doi.org/10.1016/j.jaerosci.2003.10.003, 2004.

727   Kulmala, M., Petäjä, T., Nieminen, T., Sipilä, M., Manninen, H. E., Lehtipalo, K., Dal Maso, M.,

728   Aalto, P. P., Junninen, H., Paasonen, P., Riipinen, I., Lehtinen, K. E. J., Laaksonen, A., and Kerminen,

729   V.-M.: Measurement of the nucleation of atmospheric aerosol particles, Nature Protocols, 7, 1651,

730   10.1038/nprot.2012.091, 2012.

731   Kulmala, M., Petäjä, T., Mönkkönen, P., Koponen, I. K., Dal Maso, M., Aalto, P. P., Lehtinen, K.

732   E. J., and Kerminen, V. M.: On the growth of nucleation mode particles: source rates of condensable

733   vapor in polluted and clean environments, Atmos. Chem. Phys., 5, 409-416, 10.5194/acp-5-409-2005,

734   2005.

735   Lehtinen, K. E. J., and Kulmala, M.: A model for particle formation and growth in the atmosphere

736   with molecular resolution in size, Atmos. Chem. Phys., 3, 251-257, 10.5194/acp-3-251-2003, 2003.

737   Leng, C., Zhang, Q., Tao, J., Zhang, H., Zhang, D., Xu, C., Li, X., Kong, L., Cheng, T., and Zhang,

738   R.: Impacts of new particle formation on aerosol cloud condensation nuclei (CCN) activity in Shanghai:

739   case study, Atmos. Chem. Phys., 14, 11353-11365, 2014.

740   Liu, P., Song, M., Zhao, T., Gunthe, S. S., Ham, S., He, Y., Qin, Y. M., Gong, Z., Amorim, J. C.,

34

741 Bertram, A. K., and Martin, S. T.: Resolving the mechanisms of hygroscopic growth and cloud

742 condensation nuclei activity for organic particulate matter, Nat. Commun., 9, 4076,

743 10.1038/s41467-018-06622-2, 2018.

744 Liu, P. F., Zhao, C. S., Göbel, T., Hallbauer, E., Nowak, A., Ran, L., Xu, W. Y., Deng, Z. Z., Ma,

745 N., Mildenberger, K., Henning, S., Stratmann, F., and Wiedensohler, A.: Hygroscopic properties of

746 aerosol particles at high relative humidity and their diurnal variations in the North China Plain, Atmos.

747 Chem. Phys., 11, 3479-3494, 10.5194/acp-11-3479-2011, 2011.

748 Liu, S., Hu, M., Wu, Z., Wehner, B., Wiedensohler, A., and Cheng, Y.: Aerosol number size

749 distribution and new particle formation at a rural/coastal site in Pearl River Delta (PRD) of China,

750 Atmos. Environ., 42, 6275-6283, 2008.

751 Lu, Y., Yan, C., Fu, Y., Chen, Y., Liu, Y., Yang, G., Wang, Y., Bianchi, F., Chu, B., Zhou, Y., Yin,

752 R., Baalbaki, R., Garmash, O., Deng, C., Wang, W., Liu, Y., Petäjä, T., Kerminen, V. M., Jiang, J.,

753 Kulmala, M., and Wang, L.: A proxy for atmospheric daytime gaseous sulfuric acid concentration in

754 urban Beijing, Atmos. Chem. Phys., 19, 1971-1983, 10.5194/acp-19-1971-2019, 2019.

755 Ma, N., Zhao, C., Tao, J., Wu, Z., Kecorius, S., Wang, Z., Größ, J., Liu, H., Bian, Y., and Kuang,

756 Y.: Variation of CCN activity during new particle formation events in the North China Plain, Atmos.

757 Chem. Phys., 16, 8593-8607, 2016.

758 Ma, S. S., Chen, Z., Pang, S. F., and Zhang, Y. H.: Observations on hygroscopic growth and phase

759 transitions of mixed 1, 2, 6-hexanetriol/$(NH_4)_2SO_4$ particles: Investigation of liquid-liquid phase

760 separation (LLPS) dynamic process and mechanism and secondary LLPS, Atmos. Chem. Phys.

761 Discuss., 2021, 1-18, 10.5194/acp-2020-1299, 2021.

762 Mikkonen, S., Romakkaniemi, S., Smith, J., Korhonen, H., Petäjä, T., Plass-Duelmer, C., Boy, M.,

763 McMurry, P., Lehtinen, K., and Joutsensaari, J.: A statistical proxy for sulphuric acid concentration,

764 Atmos. Chem. Phys., 11, 11319-11334, 2011.

765 Mönkkönen, P., Koponen, I. K., Lehtinen, K. E. J., Hämeri, K., Uma, R., and Kulmala, M.:

766 Measurements in a highly polluted Asian mega city: observations of aerosol number size distribution,

767 modal parameters and nucleation events, Atmos. Chem. Phys., 5, 57-66, 10.5194/acp-5-57-2005, 2005.

768 Moore, R. H., Nenes, A., and Medina, J.: Scanning Mobility CCN Analysis—A Method for Fast

769 Measurements of Size-Resolved CCN Distributions and Activation Kinetics, Aerosol Sci. Technol., 44,

861-871, 10.1080/02786826.2010.498715, 2010.

Nieminen, T., Lehtinen, K. E. J., and Kulmala, M.: Sub-10 nm particle growth by vapor condensation – effects of vapor molecule size and particle thermal speed, Atmos. Chem. Phys., 10, 9773-9779, 10.5194/acp-10-9773-2010, 2010.

Nieminen, T., Asmi, A., Dal Maso, M., Aalto, P. P., Keronen, P., Petäjä, T., Kulmala, M., and Kerminen, V.-M.: Trends in atmospheric new-particle formation: 16 years of observations in a boreal-forest environment, Boreal Environ. Res., 19 (suppl. B):191-214, 2014.

O'Dowd, C., McFiggans, G., Creasey, D. J., Pirjola, L., Hoell, C., Smith, M. H., Allan, B. J., Plane, J. M. C., Heard, D. E., Lee, J. D., Pilling, M. J., and Kulmala, M.: On the photochemical production of new particles in the coastal boundary layer, Geophys. Res. Lett., 26, 1707-1710, https://doi.org/10.1029/1999GL900335, 1999.

Ovadnevaite, J., Zuend, A., Laaksonen, A., Sanchez, K. J., Roberts, G., Ceburnis, D., Decesari, S., Rinaldi, M., Hodas, N., Facchini, M. C., Seinfeld, J. H., and O' Dowd, C.: Surface tension prevails over solute effect in organic-influenced cloud droplet activation, Nature, 546, 637-641, 10.1038/nature22806, 2017.

Paasonen, P., Nieminen, T., Asmi, E., Manninen, H. E., Petäjä, T., Plass-Dülmer, C., Flentje, H., Birmili, W., Wiedensohler, A., Hõrrak, U., Metzger, A., Hamed, A., Laaksonen, A., Facchini, M. C., Kerminen, V. M., and Kulmala, M.: On the roles of sulphuric acid and low-volatility organic vapours in the initial steps of atmospheric new particle formation, Atmos. Chem. Phys., 10, 11223-11242, 10.5194/acp-10-11223-2010, 2010.

Pajunoja, A., Lambe, A. T., Hakala, J., Rastak, N., Cummings, M. J., Brogan, J. F., Hao, L., Paramonov, M., Hong, J., and Prisle, N. L.: Adsorptive uptake of water by semisolid secondary organic aerosols, Geophys. Res. Lett., 42, 3063-3068, 2015.

Petters, M., and Kreidenweis, S.: A single parameter representation of hygroscopic growth and cloud condensation nucleus activity, Atmos. Chem. Phys., 7, 1961-1971, 2007.

Rastak, N., A. Pajunoja, J. C. Acosta Navarro, J. Ma, M. Song, D. G. Partridge, A. Kirkevåg, Y. Leong, W. W. Hu, N. F. Taylor, A. Lambe, K. Cerully, A. Bougiatioti, P. Liu, R. Krejci, T. Petäjä, C. Percival, P. Davidovits, D. R. Worsnop, A. M. L. Ekman, A. Nenes, S. Martin, J. L. Jimenez, D. R. Collins, D. O. Topping, A. K. Bertram, A. Zuend, A. Virtanen, and I. Riipinen: Microphysical

799 explanation of the RH-dependent water affinity of biogenic organic aerosol and its importance for

800 climate, Geophys. Res. Lett., 44(10), 5167-5177, doi:10.1002/2017GL073056, 2017.

801 Renbaum-Wolff, L., Song, M., Marcolli, C., Zhang, Y., Liu, P. F., Grayson, J. W., Geiger, F. M.,

802 Martin, S. T., and Bertram, A. K.: Observations and implications of liquid–liquid phase separation at

803 high relative humidities in secondary organic material produced by α-pinene ozonolysis without

804 inorganic salts, Atmos. Chem. Phys., 16, 7969-7979, 10.5194/acp-16-7969-2016, 2016.

805 Rose, C., K. Sellegri, I. Moreno, F. Velarde, M. Ramonet, K. Weinhold, R. Krejci, M. Andrade, A.

806 Wiedensohler, P. Ginot, and P. Laj: CCN production by new particle formation in the free troposphere,

807 Atmos. Chem. Phys., 17(2), 1529-1541, doi:10.5194/acp-17-1529-2017, 2017

808 Ruehl, C. R., and Wilson, K. R.: Surface organic monolayers control the hygroscopic growth of

809 submicrometer particles at high relative humidity, J. Phys. Chem. A, 118, 3952-3966, 2014.

810 Ruehl, C. R., Davies, J. F., and Wilson, K. R.: An interfacial mechanism for cloud droplet

811 formation on organic aerosols, Science, 351, 1447-1450, 2016.

812 Shen, L., H. Wang, Y. Yin, J. Chen, and K. Chen: Observation of atmospheric new particle growth

813 events at the summit of mountain Tai (1534 m) in Central East China, Atmos. Environ., 201, 148-157,

814 doi:https://doi.org/10.1016/j.atmosenv.2018.12.051, 2019.

815 Shen, X. J., J. Y. Sun, Y. M. Zhang, B. Wehner, A. Nowak, T. Tuch, X. C. Zhang, T. T. Wang, H. G.

816 Zhou, X. L. Zhang, F. Dong, W. Birmili, and A. Wiedensohler: First long-term study of particle number

817 size distributions and new particle formation events of regional aerosol in the North China Plain,

818 Atmos. Chem. Phys., 11(4), 1565-1580, doi:10.5194/acp-11-1565-2011, 2011

819 Spracklen, D. V., Carslaw, K. S., Kulmala, M., Kerminen, V. M., Sihto, S. L., Riipinen, I.,

820 Merikanto, J., Mann, G. W., Chipperfield, M. P., and Wiedensohler, A.: Contribution of particle

821 formation to global cloud condensation nuclei concentrations, J. Geophys. Res. Lett., 35, 2008.

822 Stocker, D. Q.: Climate change 2013: The physical science basis, Working Group I Contribution

823 to the Fifth Assessment Report of the Intergovernmental Panel on Climate Change, Summary for

824 Policymakers, IPCC, 2013.

825 Stolzenburg, M. R., and McMurry, P. H.: Equations Governing Single and Tandem DMA

826 Configurations and a New Lognormal Approximation to the Transfer Function, Aerosol Sci. Technol.,

827 42, 421-432, 10.1080/02786820802157823, 2008.

828   Tan, H., Xu, H., Wan, Q., Li, F., Deng, X., Chan, P. W., Xia, D., and Yin, Y.: Design and

829   Application of an Unattended Multifunctional H-TDMA System, J. Atmos. Oceanic Technol., 30,

830   1136-1148, 10.1175/JTECH-D-12-00129.1, 2013.

831   Topping, D. O., McFiggans, G. B., and Coe, H.: A curved multi-component aerosol hygroscopicity

832   model framework: Part 1 – Inorganic compounds, Atmos. Chem. Phys., 5, 1205-1222,

833   10.5194/acp-5-1205-2005, 2005.

834   Wang, S., Peng, Y., Qi, J., Wu, C., Wang, C., Wang, B., Wang, Z., Kuang, Y., Song, W., Wang, X.,

835   Hu, W., Chen, W., Shen, J., Chen, D., Shao, M., and Yuan, B.: Different chemical removal pathways of

836   volatile organic compounds (VOCs) s: Comparison of urban and regional sites, Acta Sci. Circumst., 40,

837   2311-2322, 2020. (in Chinese)

838   Wang, Z., Hu, M., Yue, D., He, L., Huang, X., Yang, Q., Zheng, J., Zhang, R., and Zhang, Y.: New

839   particle formation in the presence of a strong biomass burning episode at a downwind rural site in PRD,

840   China, Tellus B: Chem. Phys. Meteor., 65, 19965, 10.3402/tellusb.v65i0.19965, 2013.

841   Wex, H., M. D. Petters, C. M. Carrico, E. Hallbauer, A. Massling, G. R. McMeeking, L. Poulain,

842   Z. Wu, S. M. Kreidenweis, & F. Stratmann (2009), Towards closing the gap between hygroscopic

843   growth and activation for secondary organic aerosol: Part 1 – Evidence from measurements, Atmos.

844   Chem. Phys., 9(12), 3987-3997, doi:10.5194/acp-9-3987-2009.

845   Wolfe, G. M., Marvin, M. R., Roberts, S. J., Travis, K. R., and Liao, J.: The Framework for 0-D

846   Atmospheric Modeling (F0AM) v3.1, Geosci. Model Dev., 9, 3309-3319, 10.5194/gmd-9-3309-2016,

847   2016.

848   Wu, Z., Hu, M., Liu, S., Wehner, B., Bauer, S., Ma ßling, A., Wiedensohler, A., Petäjä, T., Dal

849   Maso, M., and Kulmala, M.: New particle formation in Beijing, China: Statistical analysis of a 1-year

850   data set, J. Geophys. Res., 112, D09209, 10.1029/2006jd007406, 2007.

851   Wu, Z., Birmili, W., Poulain, L., Wang, Z., Merkel, M., Fahlbusch, B., Pinxteren, D. v., Herrmann,

852   H., and Wiedensohler, A.: Particle hygroscopicity during atmospheric new particle formation events:

853   implications for the chemical species contributing to particle growth, Atmos. Chem. Phys., 13,

854   6637-6646, 2013.

855   Yu, H., Ortega, J., Smith, J. N., Guenther, A. B., Kanawade, V. P., You, Y., Liu, Y., Hosman, K.,

856   Karl, T., Seco, R., Geron, C., Pallardy, S. G., Gu, L., Mikkilä, J., and Lee, S.-H.: New Particle

857 Formation and Growth in an Isoprene-Dominated Ozark Forest: From Sub-5 nm to CCN-Active Sizes,

858 Aerosol Sci. Technol., 48, 1285-1298, 10.1080/02786826.2014.984801, 2014.

859 Yue, D., Zhong, L., Zhang, T., Shen, J., Yuan, L., Ye, S., Zhou, Y., and Zeng, L.: Particle growth

860 and variation of cloud condensation nucleus activity on polluted days with new particle formation: A

861 case study for regional air pollution in the PRD region, China, Aerosol Air Qual. Res., 16, 323-335,

862 2016.

863 Yue, D. L., Hu, M., Zhang, R. Y., Wu, Z. J., Su, H., Wang, Z. B., Peng, J. F., He, L. Y., Huang, X.

864 F., Gong, Y. G., and Wiedensohler, A.: Potential contribution of new particle formation to cloud

865 condensation nuclei in Beijing, Atmos. Environ., 45, 6070-6077,

866 https://doi.org/10.1016/j.atmosenv.2011.07.037, 2011.

867 Yue, D. L., Hu, M., Wang, Z. B., Wen, M. T., Guo, S., Zhong, L. J., Wiedensohler, A., and Zhang,

868 Y. H.: Comparison of particle number size distributions and new particle formation between the urban

869 and rural sites in the PRD region, China, Atmos. Environ., 76, 181-188,

870 https://doi.org/10.1016/j.atmosenv.2012.11.018, 2013.

871

872   FIGURE CAPTIONS

873   Figure 1. The PNSD (a), N_{CN}, N_{CCN} and AR (b), wind speed and wind direction (c), $j_{O(1D)}$, and

874   concentration of calculated H_2SO_4 (d) during the NPF event on 29th October, 2019. The blue dots in (a)

875   represents the geometric mean particle diameter (Dp_{gmd}) and the red line represents the linear fit.

876   Figure 2. Comparison of the median and interquartile κ values obtained from HTDMA and CCN

877   measurements during this campaign at Heshan, at Panyu (urban Guangzhou), and from South China

878   Sea. The κ was pointed against the corresponding median D_{50} (CCN measurement) or selected diameter

879   (HTDMA measurement). Dots represent the median values and bars represent the interquartile ranges.

880   The κ values in this measurement were obtained from HTDMA measurement (in black) and CCNc

881   measurement (ss=0.1%, 0.2%, 0.4%, 0.7%, 0.9%, and 1.0% in red and yellow for different surface

882   tensions). The yellow lines and dots represent the κ values recalculated based on $\sigma_{s/a}^{*}$. The κ values at

883   Panyu were obtained from HTDMA measurement (in purple) and CCNc measurement (ss=0.1%, 0.2%,

884   0.4%, and 0.7%, in green). The κ values from the South China Sea were obtained from CCNc

885   measurement (ss=0.18%, 0.34%, and 0.59%, in light blue). The κ values from the North China Plain

886   were obtained from HTDMA measurement.

887   Figure 3. The variation of Dp_{gmd} (blue dots), $D_{50,m}$ (yellow dots) and $D_{50,r}$ (red dots) based on pure

888   water surface tension.

889   Figure 4. The variation of N_{CCN} (a), activation ratio (b), and δ_{CCN} (c) based on the $D_{50,m}$, the $D_{50,r}$, and

890   the average D_{50}. The red line represents the measured values. The yellow line represents the values

891   calculated based on the surface tension of pure water (0.072 N m^{-1}). The purple line represents the

892   values calculated from the average D_{50}. The green region represents the interquartile values calculated

893   from the interquartile D_{50}.

894   Figure. 5 The measured and model PNSD (a and b), N_{CN} (c) and N_{CCN} (c). The blue lines in (c)

895   represent the measured values and the red lines represent the model values.

896   Figure 6. The variation of measured and model N_{CN} (a) and N_{CCN} (b) at 1.0% SS. The simulations was

897   based on standard characteristic (red solid line), halving of GR, formation rate and background particle

898   distribution (orange, purple and green solid line, respectively) and doubling of GR, formation rate and

899   background particle distribution (orange, purple and green dash line, respectively).

900   Figure 7. The number contribution (a) and its fraction (b) of CoagSnk term, CoagSrc term, GR term,

901   and formation (J) term to the N_{CCN} when it reached its peak value based under different case scenarios.

902   Figure. 8 The model N_{CCN} based on different characteristics (doubling growth rate and formation rate,

903   and halfling background particle distribution) and particle properties. Different colors and markers

904   represent case 1-9, respectively.

905   Figure 9. The measured PNSD (a, b, and c), model PNSD (d, e, and f), measured N_{CN} and model N_{CN}

906   (g, h, and i) during different NPF events. Solid and dash lines represent the measured and model N_{CN},

907   respectively.

908   Figure 10. The measured and model N_{CCN} (SS=1.0%) during different NPF events.

909   Figure 11. The measured and model N_{CN} (a) and N_{CCN} (b) on the Panyu NPF event. The bule line

910   represents the measured value. The red, yellow, purple and green lines represent the simulated N_{CCN}

911   based on standard input, growth rate of the NPF event on October 18th (refer as high GR), formation

912   rate of the NPF event on October 29th (refer as high J), and background particle distribution of the NPF

913   event on October 29th (refer as low CS PNSD), respectively.
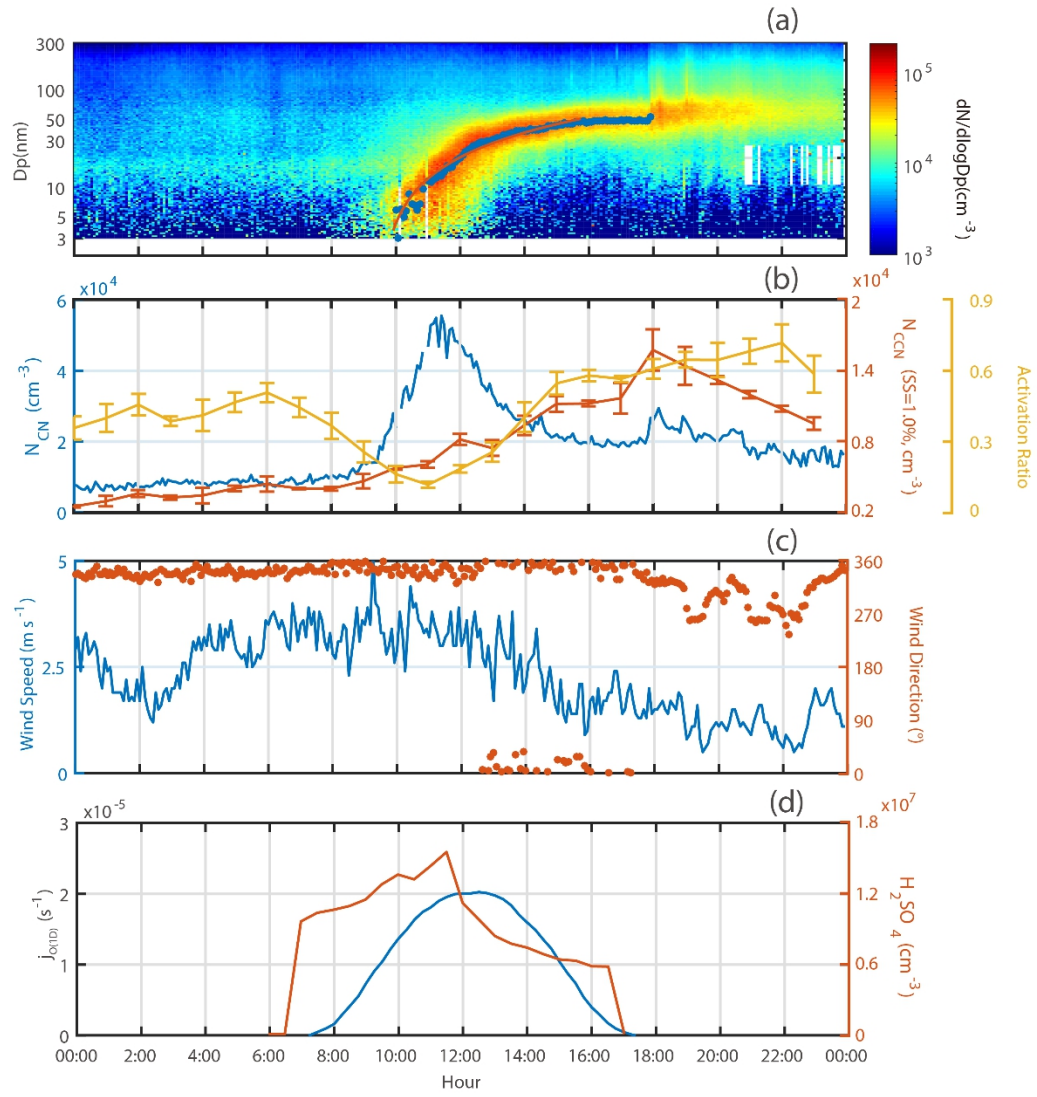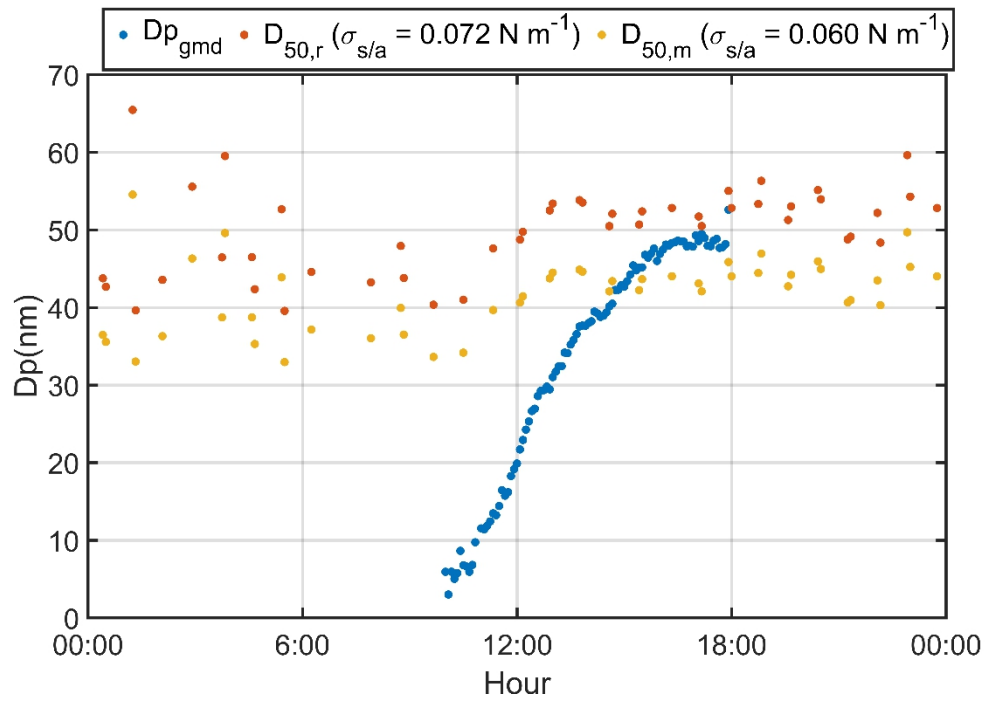
914

915 Fig. 1.

916
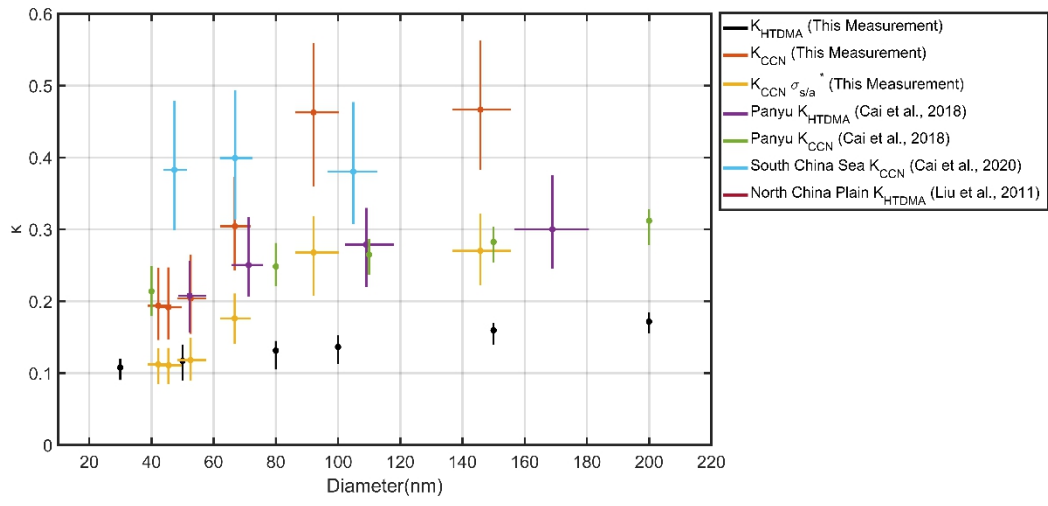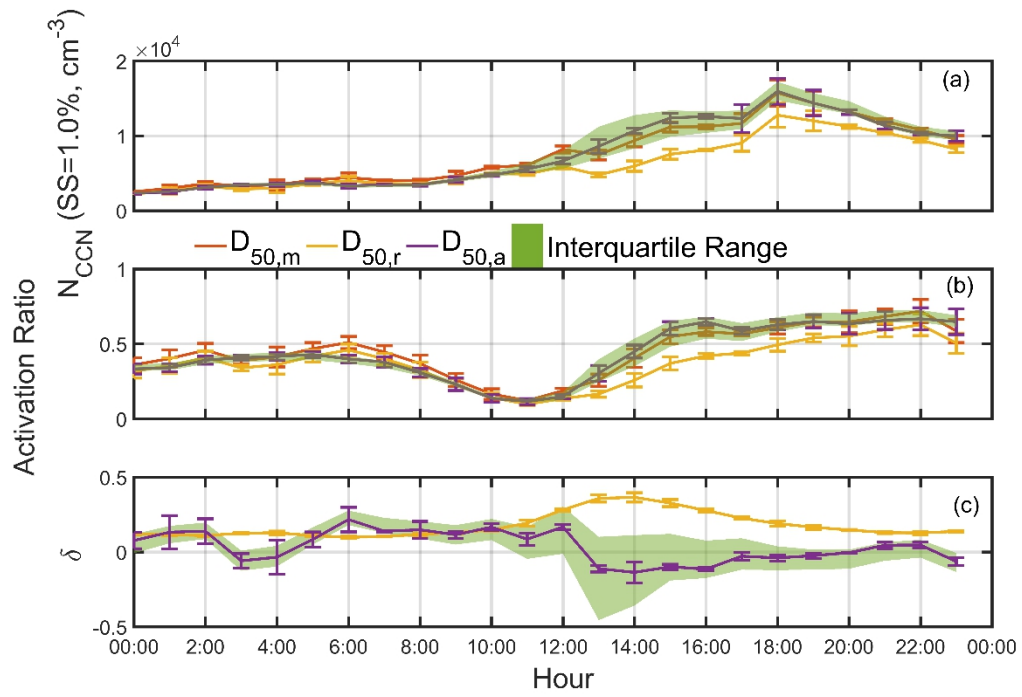
917

918

919   Fig. 2.

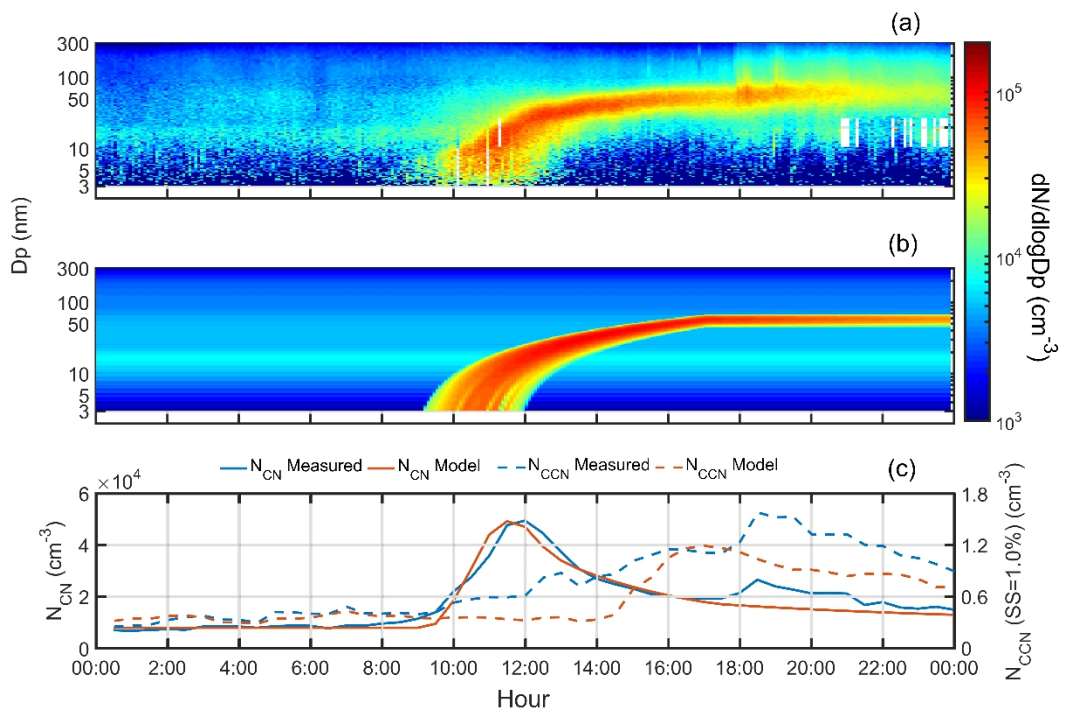920

921

922   Fig. 3.

923
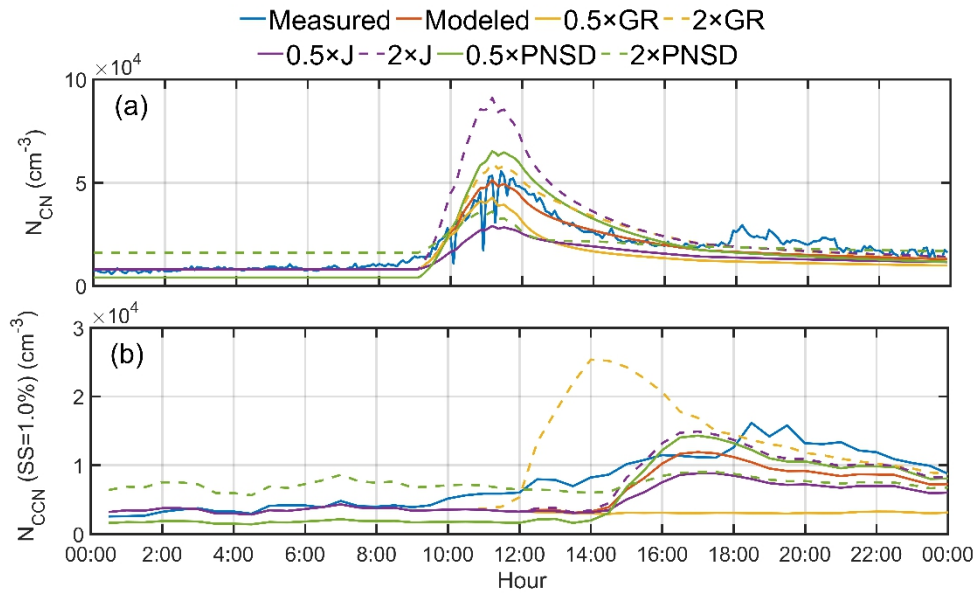
924

925

926   Fig. 4.

927
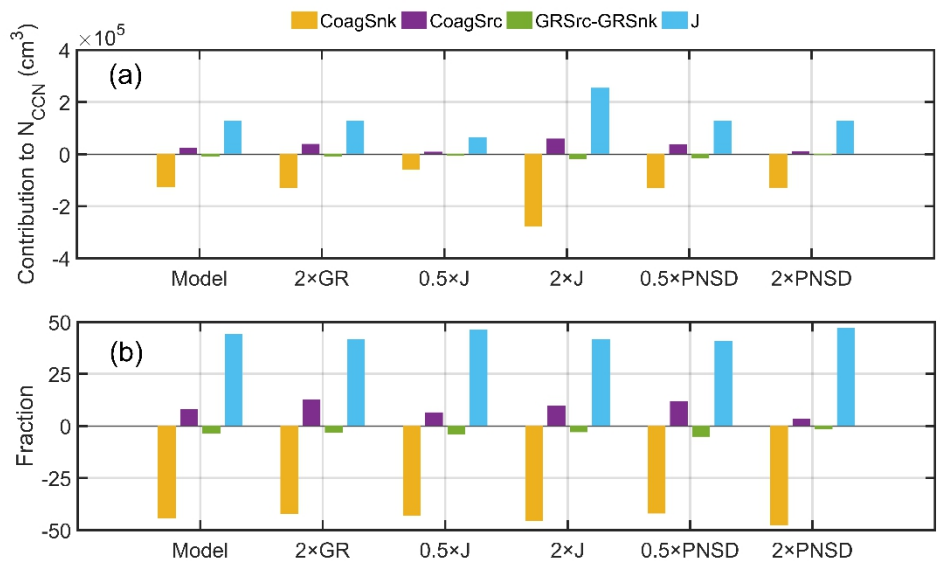
928

929

930   Fig. 5.

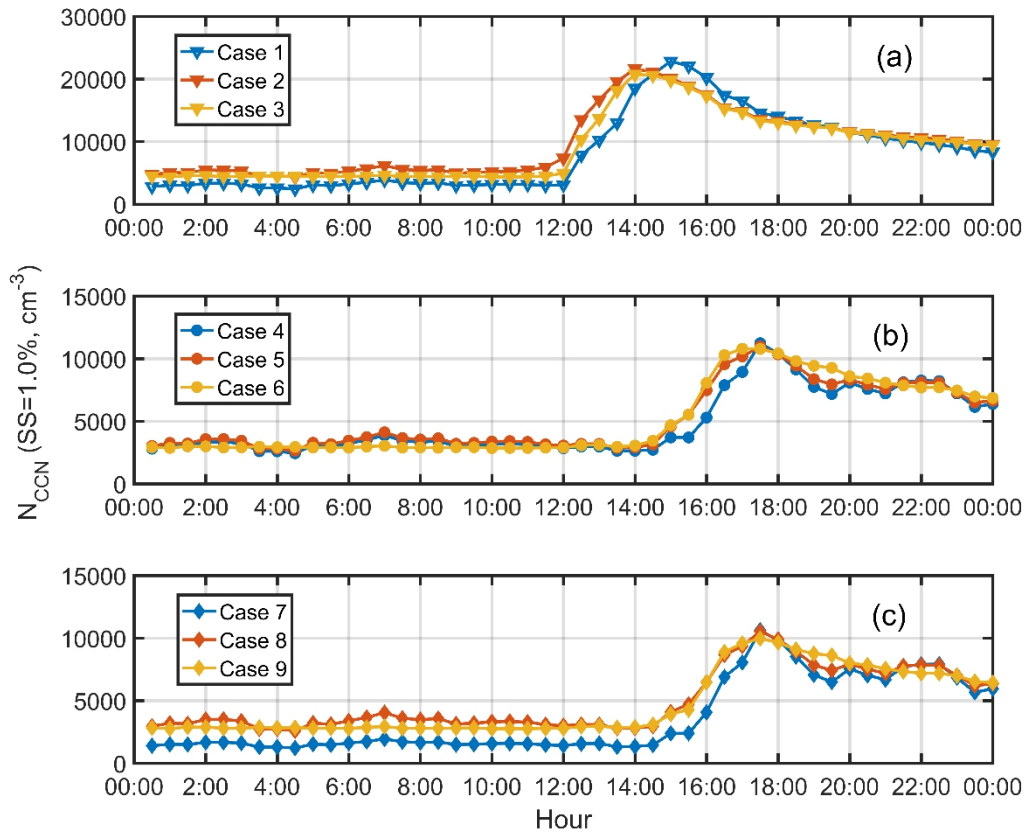931

932

933

934   Fig. 6.

935

936

937

938 Fig. 7.

939

940

941

942　　Fig. 8

943

944

945

946 Fig. 9.

947

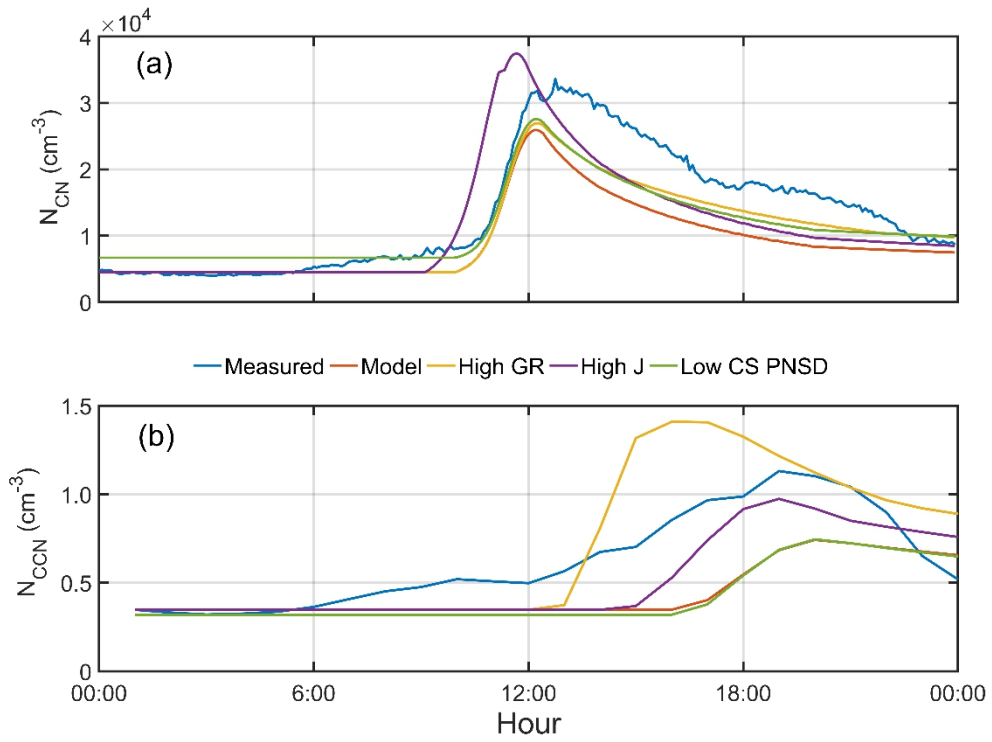2019.10.18 Heshan   2019.10.29 Heshan   2014.12.12 Panyu
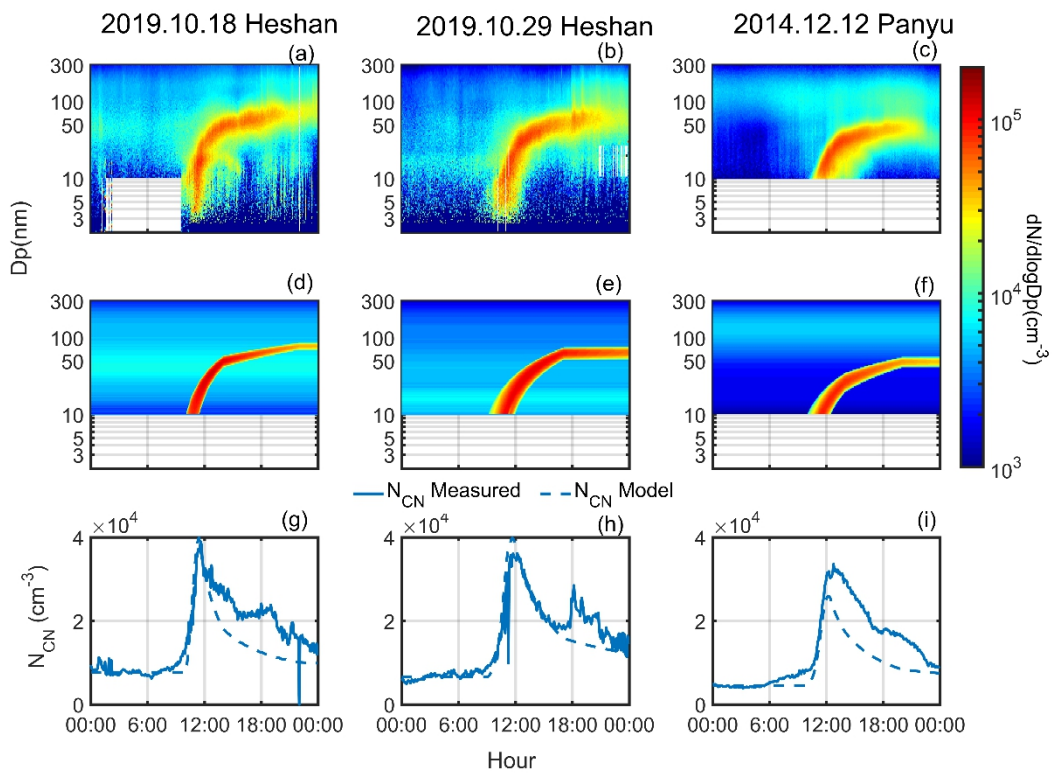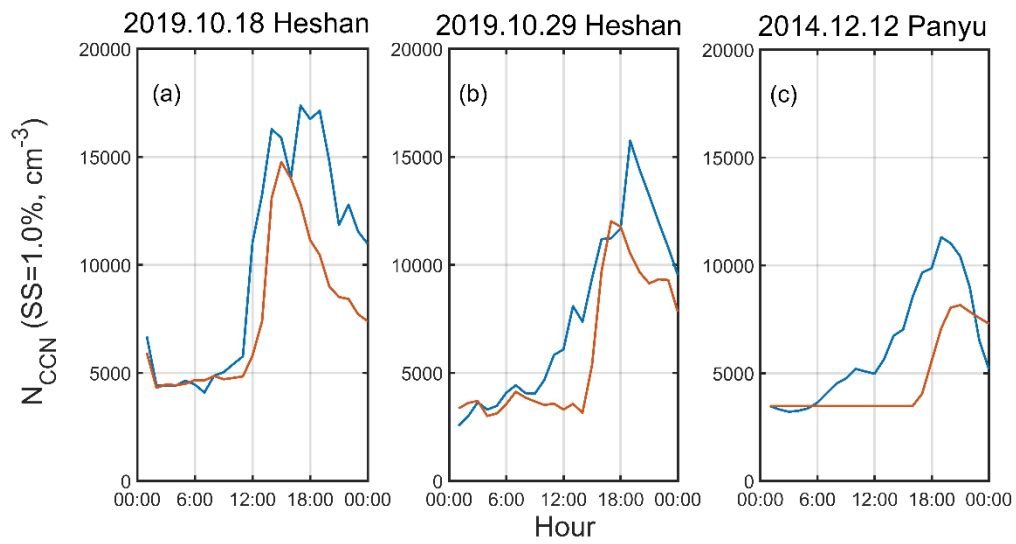
948

949

950   Fig. 10.

951

952

953

954   Fig. 11.

955